PURPOSE-LED
PUBLISHING™

PAPER • OPEN ACCESS

Thermal-electrical analogy for simulations of superconducting power cables

View the article online for updates and enhancements.

Thermal-electrical analogy for simulations of superconducting power cables

Wescley T B de Sousa[1,*] , **Dustin Kottonau**[2], **João Murta-Pina**[3] , **Antonio Morandi**[4]
and Mathias Noe[1]

[1] Institute for Technical Physics, Karlsruhe Institute of Technology, 76344 Eggenstein-Leopoldshafen, Germany
[2] Siemens Energy Global GmbH & Co. KG, 91058 Erlangen, Germany
[3] Center of Technology and Systems/UNINOVA, NOVA School of Science and Technology (FCT NOVA), Intelligent Systems Laboratory (LASI), Quinta da Torre, 2829-516 Caparica, Portugal
[4] Department of Electrical, Electronic, and Information Engineering, University of Bologna, 40136 Bologna, Italy

E-mail: sousa@kit.edu

CrossMark

Abstract

Due the integration of superconducting technologies into electrical networks around the world, its precise simulations in power grids are increasingly becoming a desirable outcome. Over the years, sophisticated methods have been used to model superconducting power cables and, in this way, predict its behavior under different conditions. Most of the available models, however, are not advisable to be used and embedded in power system simulators. In this manuscript, we focus on the development of a method specifically for modeling superconducting cables in traditional power grid simulators. We start developing the model through a case example, within the basic concepts are introduced and later expanded to general cases. The model also incorporates the transient behavior of the cooling media, which is mandatory for such cables. It has been observed that the proposed model requires less computational effort and is able to deliver accurate results when compared to more advanced methods.

Keywords: superconducting power cables, thermal-electrical analogy, transient simulations

1. Introduction

As a consequence of the increasing need for electricity worldwide, the supply of electrical energy is facing considerable challenges. The increasing insertion of renewable energy sources, as well as the associated urge to expand and modernize network structures impose major demands to network operators. In most cases, to modernize network structures such as a transmission or distribution system means to redesigning them considering the replacement of old lines with new ones. In this scenario, superconducting technologies are very attractive due to its large current carrying capacity with minimal power losses in compact geometries. Consequently, several superconducting cable projects have been deployed to demonstrate the technical feasibility of the technology [1–5] with the longest test in field experience cable so far being installed in Essen (Germany) where it remained under operation for more than 5 years without any interruption [6, 7]. Most

recently, the SuperLink project was commissioned in Munich, aiming to develop the longest 110 kV superconducting power cable ever built, with 15 km length [8]. DC superconducting cables have also gathered increased attention lately [9–12]. As example one can mention the superconducting cables for sustainable energy transition (SCARLET) project, which is bringing together 15 partners from seven countries to connect land-based remote renewable energy generation sites to the grid [13]. Likewise, in France, a DC high-temperature superconducting (HTS) cable system for railway applications under the SuperRail framework is currently under development [14].

Any project on HTS power cable relies on simulation tools to become successful. In the first stages, geometric sizes and optimized design are defined through extensive simulation runs. By means of simulations one gets detailed results of the local distributions of electromagnetic quantities and their temporal evolution. They can help estimate losses for a device under specified conditions, and also provide access to information which are difficult or even impossible to measure in experiments [15–17]. Simulation models are also useful for describing thermal performance in HTS cables, thereby helping to identify critical points for the safe operation. One of the critical issues in designing practical long-length HTS cables is their stability against fault currents, especially when it comes to their coolant temperature profiles.

A deep review regarding numerical modeling of HTS cables has been performed by Savoldi *et al* in [18], showing that several work addressing simulations of superconducting power cables are nowadays available. Different models and methods were developed over the years by considering diverse approaches. Our group itself has reported on a numerical tool based on the finite-difference method [19]. In its majority, however, all methods focus only on the cable itself, i.e. none of the model focus on the integration of such cables in power systems. It is of utmost importance to investigate the impacts caused by a HTS cable when connected to a transmission or distribution grid and several groups already attempted to conduct such a study [20–27]. In most cases, when investigating the thermal and electromagnetic behavior of HTS cables connected to power grids, one is compelled to employ very simplified models. In such models, the heat exchange between layers and the heat removal by the liquid nitrogen may not be properly considered. This happens very often, since embedding complex numerical models like finite element method (FEM) or finite difference method (FDM) in power systems simulators is not straightforward or even impossible. Besides that, such models would easily overload the computing capacity of machines.

The contribution of this work relies on the development of a suitable simulation method which has been dedicated to be embedded in usual large scale power system simulators (e.g. DIgSILENT PowerFactory, Electromagnetic Transients Program EMTP, or MATLAB Simulink). Such a simulation aims to deliver both the electrical and thermal behaviors of a HTS cable when connected to the grid and exposed to an electromagnetic transient. For that, an analogy between electrical components and thermal variables have been carried out. In 2014 our group has introduced such approach to simulate superconducting fault current limiters (SFCLs) [28] and it has been used by many research groups [29–33]. Now, based on the same principle, we propose an approach to fast thermal modeling of HTS power cables allowing improved accuracy with respect established thermal equivalent circuits. The method is based on the Mellor's equivalent thermal circuit, which is based on average values of temperature. The model considers the heat transfer between the cable layers and also is designed to predict the transient thermal behavior of the coolant media flowing inside the cable.

This paper is organized as follows: section 2 presents the HTS cable designs under consideration. Section 3 provides the background which has motivated the maturing of this simulation scheme. Here, a more simplified cable design is considered in order to better clarify why conventional lumped methods are not enough to emulate a transient thermal-behavior of a HTS cable. In section 4 the concept of Mellor's network is introduced. This concept is crucial for the formation of the subsequent networks which will be responsible for predicting temperature inside the cable. The expansion of Mellor's network to integrate the transient heating of the cooling medium is done in section 5. After presenting and detailing the construction of thermal-networks, the basic concept is applied in section 6 to build such networks for the HTS cables designs under study. Section 7 shows the electrical circuit to be solved and the simulation flow-chart to accomplish the thermal-transient. At the end, results are presented in section 8 and the conclusions are given in section 9.

2. HTS cable designs

Before proceeding with the development of the simulation method, we first introduce the cable designs which have been chosen to be taken as case studies. Two different designs were selected based on their architectures and wide consideration in projects worldwide. As it will be shown later, the boundary conditions of the model may change depending on the adopted design.

The first design considered for the model development is the three-phase concentric one, shown in figure 1(a). It consists of a cold dielectric cable, since the electrical insulation is located inside of the cryostat. In this concept all three phases are wound on a common cryostat former. Because the magnetic field compensates for itself outside of the phase positions, there is no need for a shielding. The neutral conductor is made of normal conductor (copper). The cable is cooled by sub-cooled liquid nitrogen, which is supplied to the inner corrugated tube of the cable (forward), and which returns from the cable end in the outer annular duct (return). Such a design, however, is only suitable for the medium-voltage range, as the overall cable diameter would become unacceptably large due to increased insulation thickness.
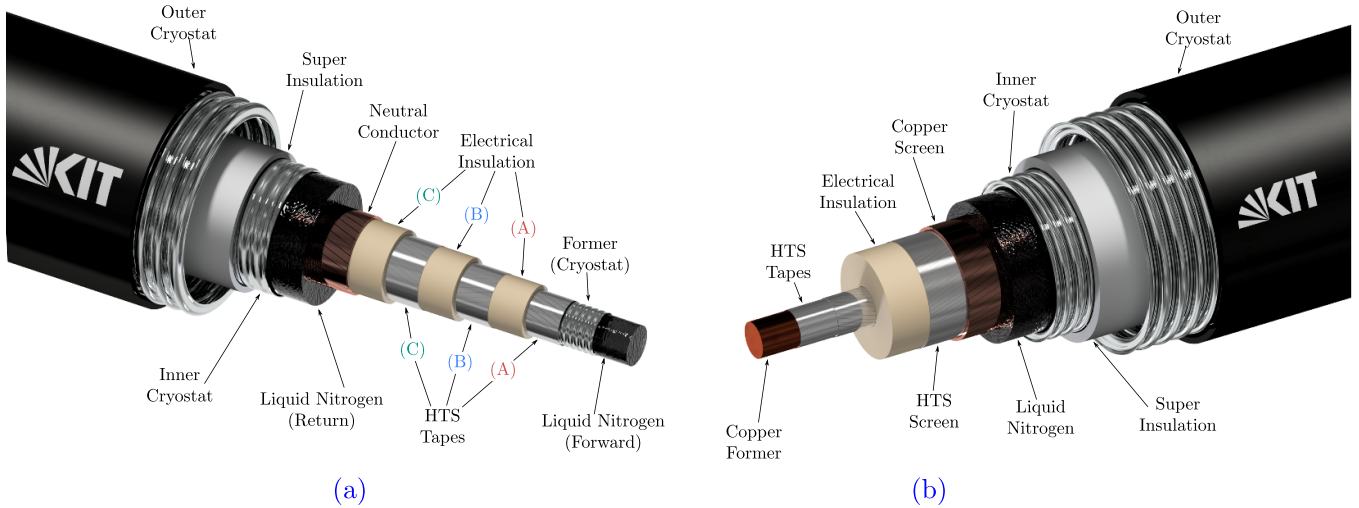
Figure 1. Schematic representation of (a) three-phase concentric and (b) single-phase superconducting power cable.

The second design is the single-phase one, shown in figure 1(b). In this design the inner layers composed of HTS tapes transmit power while the outer layers are grounded. In the outer layers, currents of equal magnitude but opposite phase to those in the inner layers are induced in the outer layers. Such induced currents completely cancel the electromagnetic fields of the inner layers. This is one of the key benefits of the cold dielectric design. The fact that the electromagnetic field is contained inside the superconducting screen also reduces the cable inductance significantly, another important benefit of the cable.

3. Background

In order to better clarify the main objective of this work, let us to consider a 1D conduction heat transfer problem in a cylindrical geometry to highlight the issues of a transient thermal simulation. As working example, consider the hollow cylinder shown in figure 2, composed by two different materials, A and B. Material A is a bad heat conductor and its thermal conductivity k_A is set to $0.15\,\mathrm{W(mK)}^{-1}$. Conversely, layer B is composed of a good thermal conductor material with a value of k_B equals to $500\,\mathrm{W(mK)}^{-1}$. The internal radius r_F is defined as 2 mm and layer A is 5 mm thick ($r_A = 7$ mm). Considering the thickness of layer B as 2.5 mm results in an outer radius r_B equal to 9.5 mm. In addition, a random length of 10 cm has been defined for this example.

For the sake of simplicity, we assume a constant temperature of 68 K at the inner and outer boundaries. In this case, considering there is no heat generation, one can ascertain that the whole cylinder body is at 68 K when in stationary regime. Such a scenario is assumed as initial condition and will change during a transient regime when a time-dependent heat generation occurs inside the layers. For instance, we assume a heat dissipation in each layer given by the curves illustrated in figure 3. Such a heat generation will certainly lead to an increase on temperature of both layers.
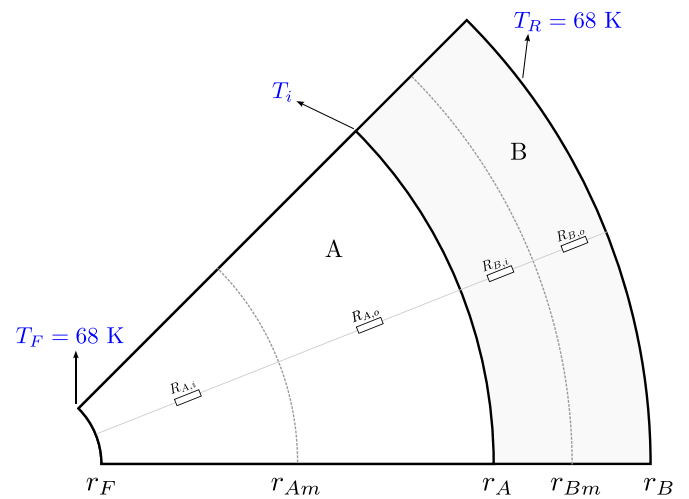

Figure 2. A sector-view of a hollow cylinder used for heat transfer analysis.

To determine temperature values over time, the solution to equation (1) must be found,

$$\frac{\rho c}{k}\frac{\mathrm{d}T}{\mathrm{d}t} = \frac{\mathrm{d}^2 T}{\mathrm{d}r^2} + \frac{1}{r}\frac{\mathrm{d}T}{\mathrm{d}r} + \frac{g}{k}. \tag{1}$$

In equation (1), k defines the thermal conductivity, c stands for specific heat, ρ represents the mass density, g is generated power per unit volume. The solution of equation (1) can be obtained through several methods. In [19], we have reported on the solution of the transient heat conduction in HTS cables by using a finite-difference method (*fdm*). Considering that such simulation method has been successfully employed in other research projects, it will be used in this manuscript as reference for comparison for the new method using thermal-electrical networks. Such an approach to simulate heat transfer phenomena is no longer a novelty and its use is widely
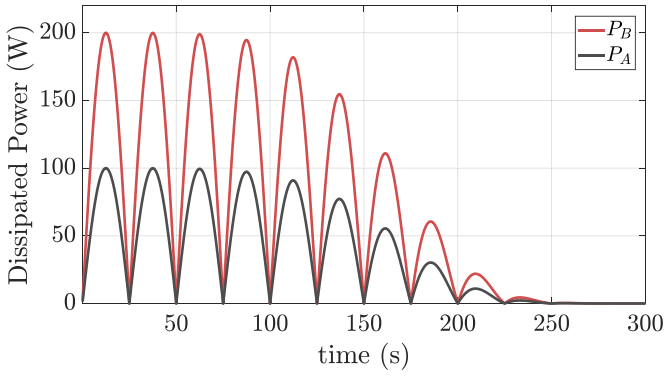
Figure 3. Time-dependent dissipated power in each layer. Curve for the analysis of the case example.

Table 1. Analogous elements between thermal and electrical systems.

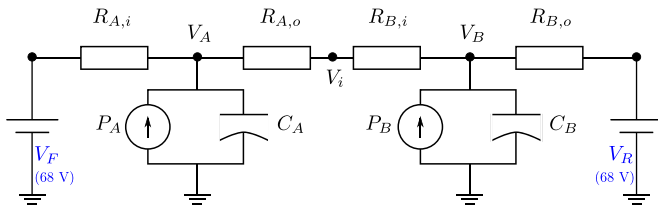| Thermal	Unit	Electrical	Unit
Temperature	K	Voltage	volt
Power	W	Current	ampere
Heat capacity	J (m$^3\cdot$K)$^{-1}$	Capacitance	farad
Conductivity	W(m$\cdot$K)$^{-1}$	Resistance	Ohm

Figure 4. Thermal-network for solution of the case example.

spread in the literature [34–37]. Table 1 lists the correspondence between thermal and electrical systems in analogous form. Basically, this method consists of setting up an electrical network with capacitors and resistors which presents a differential equation similar to equation (1) as a solution. In this way, the equivalent thermal-network, as that one shown in figure 4, can be built. Each thermal-resistor is placed at each half layer and the temperature values are obtained by calculating the voltages V_A and V_B at the indicated nodes. In general, thermal-resistors and capacitors for cylindrical geometries are defined in regular textbooks of heat conduction [36, 38] according to equation (2),

$$R = \frac{\ln(r_{ot}/r_{in})}{2\cdot\pi\cdot k\cdot L} \tag{2}$$

$$C = \rho\cdot c\cdot V. \tag{3}$$

In equation (2), r_{ot} and r_{in} designate the outer and inner radius of a half layer. Parameter L gives the length of the hollow cylinder. The capacitors in figure 4 represent the thermal capacity of the layers and their values are given by equation (3), where V stands for volume. Variables P_A and P_B are current sources placed at the center of the layers which
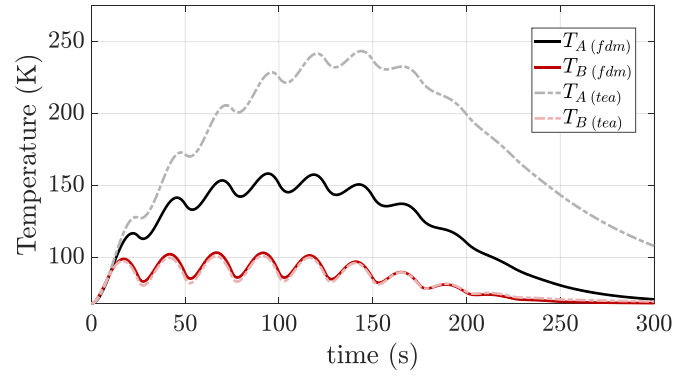

Figure 5. Temperature values at the center of the layers obtained for the case example. Comparison between the thermal-electrical analogy (*tea*) and finite-difference method (*fdm*).

emulate the heat dissipation in the layers obtained from the curves shown in figure 3.

Figure 5 presents the dynamic behavior of temperatures at the center of layers A and B. Plotted are the results obtained by the thermal electrical analogy network (*tea*) illustrated in figure 4 compared with the results achieved by means of finite-difference method (*fdm*). It is very apparent that the thermal electrical analogy model does not deliver correct results. Although the shape of the curve for the temperature of layer A follows a similar pattern, it still differs too much from the correct curve given by the *fdm* model and cannot be seen as a satisfactory outcome. This result tends to be even worst in case of a multi-layered cylinder bodies.

The results discrepancy shown in figure 5 has two main reasons. In the first place, the error lies in assuming that the distributed losses can be lumped into a single heat flux source at the center of the layer. In the case of cylindrical geometries the heat flux along the radial direction is not constant, since the traversal area changes along the radius. Therefore, a concentrated current source to emulate the heat losses will lead to inaccurate results. Secondly, that definition for the thermal resistor given by equation (2) originates from the assumption that there is no heat generation inside the cylinder body. Because we seek for the solution of heat transfer inside cylindrical geometries with internal energy dissipation, that definition for the thermal-resistor must be disregarded.

Modeling heat transfer in solid bodies by means of thermal networks is a common practice in many fields of engineering, including permanent magnets synchronous motors. Different research groups have investigated how to properly build such a network to correct the overestimated temperature values [39–43]. In 2019, Su *et al* developed a thermal-network to simulate HTS power cables [44] in electrical grids. In that work, thermal-resistors are defined based on the finite-difference method and consider the heat generation as a concentrated current source. The model delivers good results when compared with COMSOL (FEM) simulations, but it may fail if the thickness of the cable layers increases.

The most appropriate thermal-network to simulate transient heat transfer in cylindrical bodies seems to be that one proposed by Mellor *et al* in [45]. The authors managed to show

that the internal heat generation is applied correctly by adding a negative resistance in the network. The derivation of general cylindrical components is discussed next.

4. The Mellor network

4.1. Hollow cylinder

The thermal-network proposed by Mellor *et al* in [45] has long been adopted as a reference by researchers working on induction motor thermal calculations [46–49]. Differently from the usual thermal-analogy found in textbooks, the Mellor network does not provide local values, but mean values of temperature instead. In this section, the basic concepts of the Mellor's network for hollow geometries are introduced. We shall later expand it to full cylinders and further include the temperature calculation of the cooling media.

Let us assume once again the case example of the previous section and for instance focus only on one single layer. In order to properly determine the components of the electrical network, we can consider the steady-state solution of equation (1), i.e. making $dT/dt = 0$. Performing the integration of equation (4) over the volume yields the mean temperature value $T_{m,A}$ of layer A,

$$T_{m,A} = \frac{1}{V_A} \int_{r_F}^{r_A} \int_0^{2\pi} \int_0^L T_A(r) \cdot r \cdot dr \cdot d\theta \cdot d\ell. \quad (4)$$

In equation (4), $T_A(r)$ is the general solution form for the steady state of equation (1) and it is given by,

$$T_A(r) = c_1 \ln(r) - \frac{P_A \cdot r^2}{4 \cdot k_A \cdot V_A} + c_2 \quad (5)$$

where c_1 and c_2 are constants which can be calculated by applying the boundary conditions: $T(r_F) = T_F$ and $T(r_A) = T_i$. Hence:

$$c_1 = \frac{1}{\ln(r_A/r_F)} \left[(T_i - T_F) + \frac{P_A}{4 \cdot k_A \cdot V_A} \cdot (r_A^2 - r_F^2) \right] \quad (6)$$

$$c_2 = \frac{T_F \cdot \ln(r_A) - T_i \cdot \ln(r_F)}{\ln(r_A/r_F)}$$
$$+ \dots \frac{P_A}{4 \cdot k_A \cdot V_A} \cdot \left[\frac{r_F^2 \cdot \ln(r_A) - r_A^2 \cdot \ln(r_F)}{\ln(r_A/r_F)} \right] \quad (7)$$

Now, knowing c_1 and c_2, one can replace equation (5) in (4) to obtain the analytical formula for the mean temperature value $T_{m,A}$ at the steady state regime,

$$T_{m,A} = T_i \cdot \left[\frac{r_A^2}{(r_A^2 - r_F^2)} - \frac{1}{2 \cdot \ln(r_A/r_F)} \right]$$
$$+ \dots T_F \cdot \left[\frac{1}{2 \cdot \ln(r_A/r_F)} - \frac{r_F^2}{(r_A^2 - r_F^2)} \right]$$
$$+ \dots P_A \cdot \left[\frac{(r_F^2 + r_A^2)}{8 \cdot k_A \cdot V_A} - \frac{(r_A^2 - r_F^2)}{8 \cdot k_A \cdot V_A \cdot \ln(r_A/r_F)} \right]. \quad (8)$$
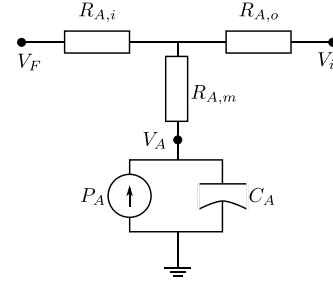

Figure 6. Mellor's thermal network for a hollow cylinder. Circuit for layer A only.

Differently from equation (5), which provides the distribution of temperature values inside the domain of layer A, equation (8) only provides a single value for the same domain that represents an overall mean temperature.

Mellor's thermal-network consists of a 'T' circuit, similar to that one shown in figure 4 but with an additional resistor right after the point where the voltage of interest is calculated. Figure 6 illustrates such a network for layer A of the case study. In this network, the voltage at the point V_A is the analogy to the mean temperature $T_{m,A}$. By means of equation (9), one can determine the voltage V_A in steady state,

$$V_A = V_i \cdot \left[\frac{R_{A,i}}{R_{A,i} + R_{A,o}} \right] + V_F \cdot \left[\frac{R_{A,o}}{R_{A,i} + R_{A,o}} + \right]$$
$$\dots P_A \cdot \left[R_{A,m} + \frac{R_{A,i} \cdot R_{A,o}}{R_{A,i} + R_{A,o}} \right]. \quad (9)$$

The equivalent circuit of the two materials problem presented in figure 2 is shown in figure 7. This is obtained by coupling together the equivalent circuits of figure 6 for materials A and material B. In order to make the thermal-network of figure 7 valid to calculate the mean temperature $T_{m,A}$ of layer A, one must correctly determine the resistors $R_{A,i}$, $R_{A,o}$ and $R_{A,m}$. This can be achieved by a comparison between the terms of equations (8) and (9). As a result one gets the following set of equations:

$$R_{A,i} = \frac{1}{4 \cdot \pi \cdot k_A \cdot L} \cdot \left[1 - \frac{2 \cdot r_A^2 \cdot \ln(r_A/r_F)}{(r_A^2 - r_F^2)} \right] \quad (10)$$

$$R_{A,o} = \frac{1}{4 \cdot \pi \cdot k_A \cdot L} \cdot \left[\frac{2 \cdot r_F^2 \cdot \ln(r_A/r_F)}{(r_A^2 - r_F^2)} - 1 \right] \quad (11)$$

$$R_{A,m} = \frac{-1}{8 \cdot \pi \cdot (r_A^2 - r_F^2) \cdot k_A \cdot L} \cdot \left[r_A^2 + r_F^2 \right.$$
$$\left. - \dots \frac{4 \cdot r_F^2 \cdot r_A^2 \cdot \ln(r_A/r_F)}{(r_A^2 - r_F^2)} \right]. \quad (12)$$

As can be seen, thermal-resistors are given in terms of the dimensions of the cylindrical layer and its thermal conductivity. The negative value $R_{A,m}$ (equation (12)) acts as a correction for the high temperature values, which normally arise from such a thermal-network. Although the thermal-resistors have been defined for the steady state, equations (10)–(12) are also
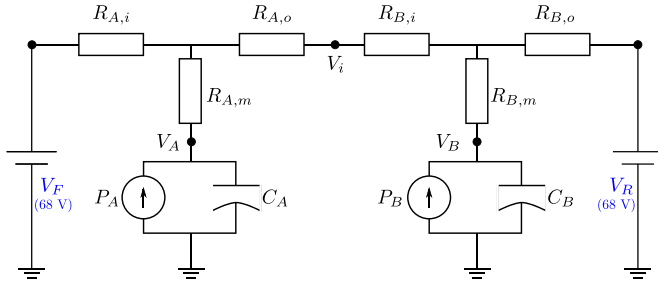
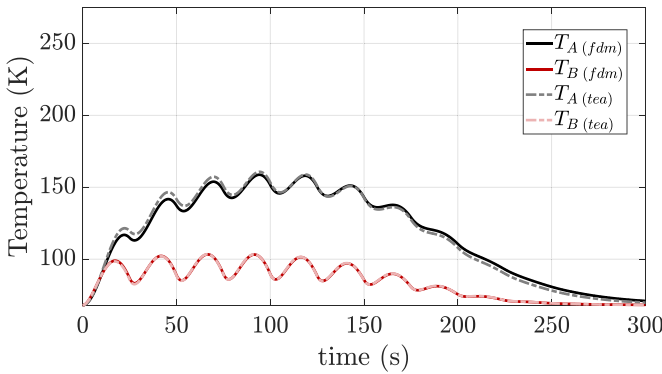**Figure 7.** Mellor's thermal network for solution of the case example.

Figure 8. Temperature mean values using Mellor's network for the case study. Comparison between the thermal-electrical analogy (*tea*) and finite-difference method (*fdm*).
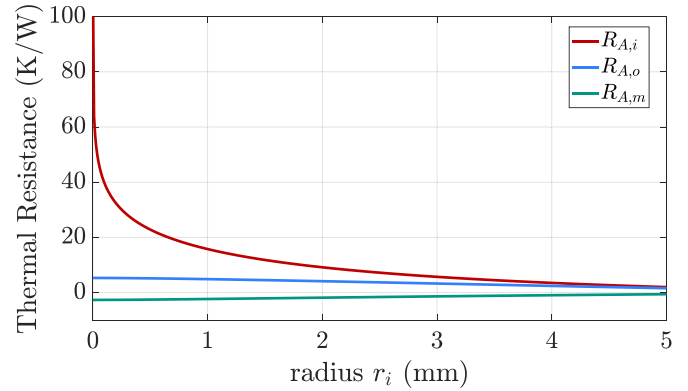

Figure 9. Behavior of the thermal resistance values when the internal radius tends to zero. Analysis for the full cylinder model.
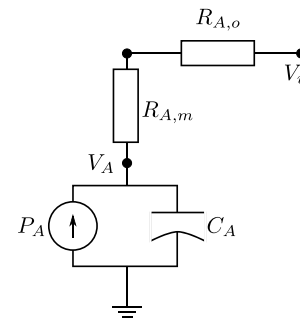

Figure 10. Thermal network for the core of a full cylinder.

$$\lim_{r_F \to 0} R_{A,m} = \frac{-1}{8 \cdot \pi \cdot k_A \cdot L}. \tag{15}$$

Because there is no heat flux towards the center of the full cylinder, the resistance $R_{A,i}$ tends to infinity. The two remaining thermal resistors tend to constant values, given by equations (14) and (15). As a result, that thermal circuit shown in figure 10 can be used to model the core of a full cylinder.

4.3. Multilayer concept

Although the results achieved with the Mellor's network are in good agreement with those obtained by finite-difference method, it is still possible to observe some discrepancies between the results of the two models. It is important to highlight that such a thermal-network was initially developed for transient simulations of induction motors, which are at the most composed of metallic materials with good thermal conductivity. In other words, the model should work well if no significant temperature gradient takes place inside a particular layer.

In layer B of the proposed case example almost no temperature gradient exists, whereas a noticeable one occurs inside layer A (figure 11). That is the reason why some discrepancy between the thermal-electrical analogy (*tea*) and finite-difference method (*fdm*) can be observed for layer A, as it is shown in figure 8. Although the discrepancies are not harsh, such a behavior tends to become worse in cases where several layers and different materials are considered, as is exactly the

valid for transient conditions. In this case, however, a component representing the thermal capacitance is added at the mean temperature node in order to model the heat stored in the layer. Such capacitance is defined according to equation (3). With the same approach one can build a similar thermal-network for layer B. Hence, for the considered case example, that network illustrated in figure 7 can be assembled.

Figure 8 compares mean temperature values for the case example achieved with finite-difference method and that Mellor's network shown in figure 7. In comparison with those results shown in figure 5, a better match has been found by using Mellor's network. Such a thermal-network covers in a proper way the boundary conditions and heat generation and is well suited for the thermal modeling of cylindrical geometries.

4.2. Full cylinder

The thermal resistors accomplished by the Mellor's network are suitable for hollow cylinders and can be deployed to simulate three-phase concentric HTS power cables. Since we also intend to simulate single-phase cables, as that one illustrated in figure 1(b), a model for this design must be addressed. Figure 9 and equations (13)–(15) show the behavior of the thermal-resistances of layer A when $r_F \to 0$,

$$\lim_{r_F \to 0} R_{A,i} = \infty \tag{13}$$

$$\lim_{r_F \to 0} R_{A,o} = \frac{1}{4 \cdot \pi \cdot k_A \cdot L} \tag{14}$$
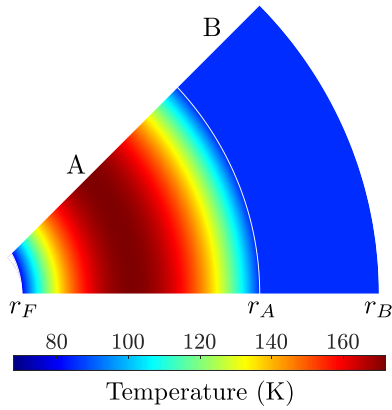
Figure 11. Temperature distribution for the case example at $t = 150$ s. Results obtained by means of the finite-difference method.
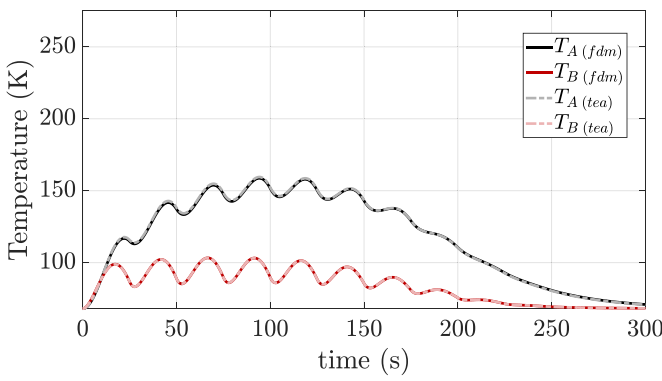

Figure 12. Temperature mean values using Mellor's network for the case example when layer A is divided into five sub-layers. Comparison between the thermal-electrical analogy (*tea*) and finite-difference method (*fdm*).

case when simulating HTS power cables. To overcome such an issue, it is reasonable to divide those layers with large thickness or low thermal conductivity into sub-layers. The lower is the thermal conductivity or the larger is the thickness of a certain layer, the higher will be the number of necessary sub-layers. An optimum number is reached when the calculated temperature does not change with the increase of sublayers.

Figure 12 shows the results for the case example when dividing layer A into five sub-layers. Thus, in this case, a total number of six layers were considered (one for layer B and five for layer A). Just for reference, the finite-difference method required a total of 7502 elements to reach a satisfactory result. Hence, even though it may be necessary to divide the geometry of interest into more sub-layers, the thermal-electrical analogy model needs much less subdivisions to provide a reliable result. Dividing the geometry into sub-layers will be necessary when simulating HTS power cables.

5. Cable cooling

In order to further extend the concepts of the Mellor's network to be used in simulation of HTS power cables, we must now include the heat exchange with the cooling media. Aiming to
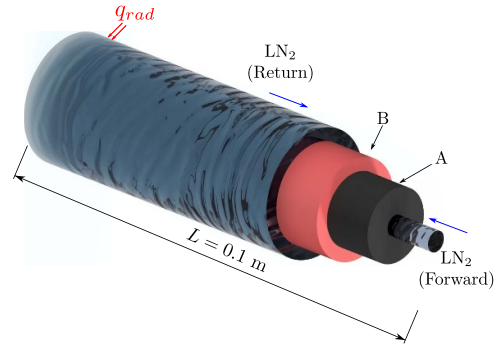

Figure 13. Extension of the case example study in a 2D problem to include cooling media.

better clarify the development of the whole model, let us now expand the case example to a 2D problem with liquid nitrogen flowing forth and back in the assembly (a similar concept to that one used in the three-phase concentric HTS cables). Figure 13 illustrates the new configuration of the case study with a heat input q_{rad} on the return flow of the liquid nitrogen. The geometric sizes remains the same as before.

So far, only the heat conduction along radial direction has been covered. Although the heat conduction along the axial direction in the solid layers of the cable exists, its effect is minor when compared to the radial heat conduction. Naturally, when considering superconducting cables composed by inhomogeneous tapes, the axial heat conduction must be considered. In the first step of this work however, no variations of the critical current along length have been considered and, therefore, the axial heat conduction in the solid layers will be neglected.

In the case of the cooling media inside the cable, however, the axial heat transfer has a major effect. Because the cooling is circulating inside the cable cryostat, it transports heat more easily along the length. Thus, such a phenomena must be included in the features of the thermal network for the simulations of the transient behavior. This is achieved by dividing the length of the cable into Δz elements. For each Δz element along the length, a thermal network is build (figure 14). In the next sections the inclusion of the convective heat transfer and heat conduction along the length performed by the cooling media is described.

5.1. Convective heat transfer

The convective heat transfer between the solid boundaries and cooling medium free stream can be modeled by a single thermal contact resistance. In figure 14, resistance $R_{\mathrm{c},F}$ models the convective heat transfer between layer A and the forward flux of the liquid nitrogen, whereas $R_{\mathrm{c},R}$ represents the heat transfer between layer B and the return flow of the cooling. These resistors are given by equation (16),

$$R_{\mathrm{c}} = \frac{1}{h_{\mathrm{c}} \cdot A_{\mathrm{c}}}. \tag{16}$$

Constant A_{c} is the area of contact surface between solid layer and fluid. Parameter h_{c} is the heat transfer coefficient

which is in general based on correlations that are derived experimentally for many technical configurations and is formulated with a dimensionless Nusselt number, the thermal conductivity of the fluid and the diameter of the pipe. The correlation for the Nusselt number in pipe flow is found in [50], which is a fully developed turbulent flow for the operating mass flow and the pipe diameter. The correlation is a function of temperature and pressure, where the influence of the pressure can be neglected in the range of the operating condition of liquid nitrogen.

5.2. Cooling media

Because the temperature of the cooling medium has a crucial impact on the behavior of the HTS cable and its temperature will not remain constant in case of a transient event, we must include it in the thermal-network. In figure 14 the equivalent thermal circuits corresponding to the return and forward flows of liquid nitrogen are highlighted by square boxes. They are connected to the solid layers of the cable through the thermal convective heat transfer resistors described in section 5.1. As in the solid layers, the capacitors represent the stored heat and can be calculated by means of equation (3). For the return flow, a current source related to the external radiation P_{rad} per meter is attached to the network.

Resistors R_L and the controlled voltage sources at both extremities of the network rise from the governing differential equation which describes the heat transfer by convection in the forced LN_2 flow inside a pipe. Equation (17) describes the axial heat transport for the return flow,

$$\rho c \frac{\mathrm{d}T_R}{\mathrm{d}t} - \rho c v_R \frac{\mathrm{d}T_R}{\mathrm{d}z} = \frac{h_c \cdot U_R \left(T'_B - T_R \right)}{A_R} + \frac{q_{\mathrm{rad}}}{A_R}. \quad (17)$$

Sub-index R describes quantities related to the return flow. U_R indicates the outer perimeter and A_R denotes the cross-section area of the pipe. T'_B indicates the temperature of layer B at the interface which exchanges heat with the fluid and q_{rad} denotes the heat load that reaches the liquid nitrogen inside the pipe. In equation (17), the velocity of the fluid v_R has a negative signal, since it accounts for the return of the cooling media. The next steps are identical for the forward flow, but with a positive signal for the fluid's velocity and with no heat load ($q_{\mathrm{rad}} = 0$). It is worth to mention that equation (17) derives from an energy balance and, therefore, delivers a medium value of temperature for the fluid. In this way, there is no need to calculate a mean value using that integral shown in equation (4).

As already mentioned, the heat transported by the cooling media along the cable length should not be neglected. For this reason, a discretization over the axial direction of the cable can be done. Using the finite-difference method to discretize equation (17) in Δz elements along the length in stationary regime results in:

$$T_{R,z} = \frac{\Gamma}{(1+\Gamma)} \cdot T'_B - \frac{1}{(1+\Gamma)} \cdot T_{R,z-1} + \frac{\Psi}{(1+\Gamma)} \cdot q_{\mathrm{rad}}. \quad (18)$$
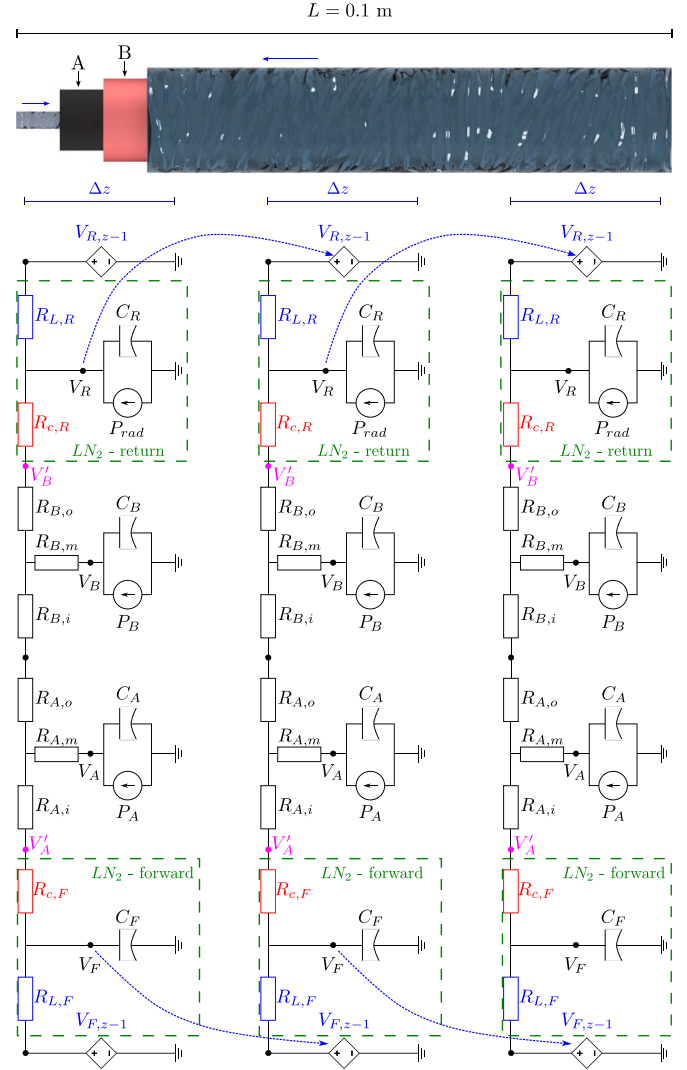
Figure 14. Thermal networks representing the radial heat transfer in each Δz element along the length.

In equation (18), the fluid velocity was replaced by that relation given in (19), which relates it to the pipe cross section area A and the mass flow rate $\dot{m}$. This leads to the definition of Γ and Ψ according to equations (20) and (21), respectively,

$$v = \frac{\dot{m}}{\rho \cdot A} \quad (19)$$

$$\Gamma = \frac{\Delta z \cdot U \cdot h_c}{\dot{m} \cdot c} \quad (20)$$

$$\Psi = \frac{\Delta z}{\dot{m} \cdot c}. \quad (21)$$

In figure 14, the voltage at the V_R node represents the temperature of the fluid. The voltage source $V_{R,z-1}$ at the extremity takes the values of the previous network in order to emulate the heat transported by the cooling medium. Taking the thermal conductances G in the 'T' circuit, which represents the return flow ($G = 1/R$), one can calculate V_R as follows:

$$V_{R,z} = \frac{G_{c,R}}{(G_{c,R} + G_{L,R})} \cdot V_B' - \frac{G_{L,R}}{(G_{c,R} + G_{L,R})} \cdot$$
$$V_{R,z-1} \ldots + \frac{1}{(G_{c,R} + G_{L,R})} \cdot P_{\text{rad}}. \tag{22}$$

Making $P_{\text{rad}} = dz \cdot q_{\text{rad}}$ and comparing equations (18) and (22) term by term yields to the general relation for R_L:

$$R_L = \frac{1}{\dot{m} \cdot c}. \tag{23}$$

With the definitions of the thermal resistances given by equations (16) and (23), the convective heat exchange and dynamical heating of the cooling fluid can be integrated in the simulations of HTS power cables. In the next sections, the main concepts presented so far will be used to build the thermal network for those designs presented in figure 1.

6. Thermal network for HTS cables

The aforementioned and developed methodologies will now be applied to build thermal networks for those HTS cable designs depicted in figure 1. In this work we do not focus on the performance of HTS cables or on the optimization of operational parameters, provided it has been already investigated several times by many research groups. We rather focus only on the development of an equivalent circuit model for possible use in power system simulations and the parameters here assumed are quasi-arbitrary. With that in mind, we assume that both designs have the same type of HTS tape, with the same values of critical current. In the same way, the geometrical sizes (tables 3 and 5) are only for model development purposes and naturally can be consequently adapted according to project requirements.

In the upcoming sections, all tapes are assumed to be 4 mm wide with a critical current of 200 A at 77 K. In addition, it is necessary to assume that the HTS tapes are densely wounded, enabling to assume the cable as a homogeneous cylinder. If a non-negligible space between the tapes exists, the proposed approach may fail. As operational data, we have assumed for both cable designs a mass flow rate of $0.4\,\text{kg s}^{-1}$ and an input temperature of 68 K for the liquid nitrogen. The simulation domain is set only until the inner cryostat, since at this edge the external radiation has been set as boundary condition ($1.7\,\text{W m}^{-1}$). It must be pointed out that despite the HTS layers may be composed by multiple tapes, they are modeled as unique annular volume. This means that all tapes of one layer are assumed to be at the same temperature and no azimuthal heat transfer between tapes is considered in the model. The same consideration holds for the copper tapes of the neutral conductor or the screen. For the finite-difference model (*fdm*) and thermal-analogy model (*tea*), the whole length of the cables (1 km) has been divided into discretized elements $\Delta z = 10\,\text{m}$. The time was discretized in $\Delta t = 0.1\,\text{ms}$. Table 2 lists the specific heat c, density ρ, and thermal conductivity k of each material used in the simulations.

Table 2. Physical parameters used in the simulations.

Material	c (J(kgK)$^{-1}$)	ρ (kg m^{-3})	k (W(mK)$^{-1}$)
LN$_2$	2025	811	0.15
Stainless Steel	200	7900	1.0
HTS Tape	217	9000	150
PPLP	430	1098	0.15[a]
Polycarbonate	1200	1210	0.22
Copper	244	8960	534.2

[a] Because the electrical isolation is immersed in LN$_2$, one assumes its thermal conductivity is the same of the coolant.

Table 3. Three-phase concentric cable sizes.

	Value	Unit	Property
Former	17	mm	Radius
Internal cryostat	18	mm	Radius
HTS tapes	0.2	mm	Thickness
Electrical insulation	3.0	mm	Thickness
Neutral conductor	3.0	mm	Thickness
Inner cryostat	60	mm	Radius
Cable length	1.0	km	Length

6.1. Three-phase concentric

Table 3 lists the geometric sizes of the three-phase concentric design assumed for simulation. In this cable 22 tapes are arranged in phase A, whereas 26 tapes are needed for phase B and 30 tapes for phase C. Assuming the geometry of the three-phase concentric design presented in figure 1(a), one can build the thermal-network illustrated in figure 15 for each Δz element along the cable length. For this network, the temporal solution can be obtained by solving the matrix differential equation (24),

$$\mathbf{A_3} \times \mathbf{C_3} \times \dot{\mathbf{V}}_3 = \mathbf{H_3} + [\mathbf{Y_3} \times \mathbf{V_3}] + [\mathbf{A_3} \times \mathbf{P_3}]. \tag{24}$$

Each matrix of equation (24) is presented in details in appendix A. Such matrices are obtained by applying Kirchhoff's current law at each node where the voltage is supposed to be calculated. Figure 15 and equation (24), however, describe the case where no sub-layers are considered. To assure a better precision instead, the multilayer concept described in section 4.3 must be applied. In this case, the thermal-network of figure 15 and those matrices in appendix A must be accordingly expanded. Table 4 presents the necessary radial discretization of the simulation domain to ensure the precision for each method used.

6.2. Single-phase

With respect to the single-phase cable, 10 HTS tapes transports the nominal current and 14 HTS tapes composes the shielding layer. Geometric sizes for the considered design are listed on table 5. Figure 16 represents the thermal-network for the single-phase design, which can be solved through equation (25),
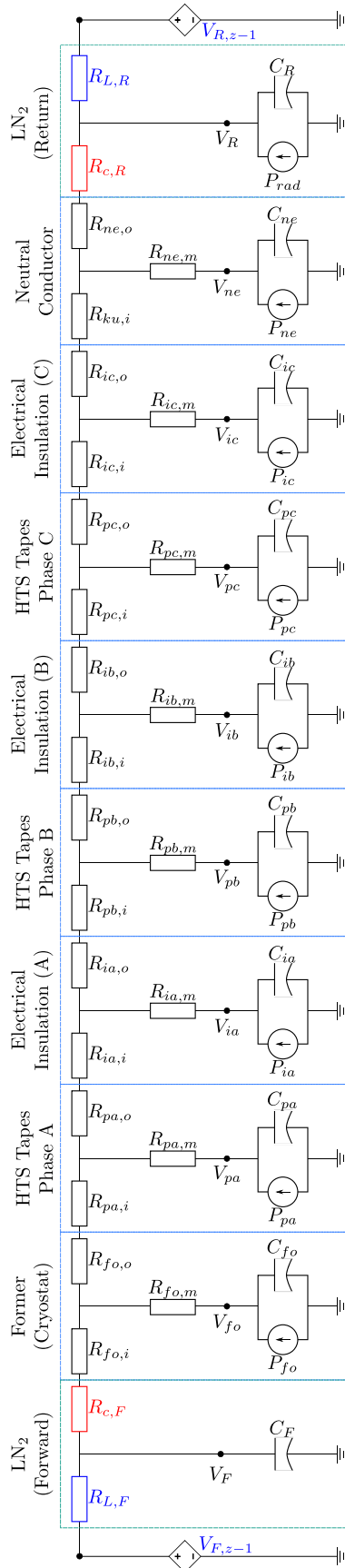
Figure 15. Thermal-network for the three-phase concentric HTS cable design.

Table 4. Discretization of the three-phase concentric design along radial direction.

Layer	Number of elements	
	fdm	*tea*
Former	150	8
HTS tapes	30	1
Electrical insulation	450	15
Neutral conductor	555	2

Table 5. Single-phase cable sizes.

	Value	Unit	Property
Copper former	5.5	mm	Radius
HTS tapes	0.2	mm	Thickness
Electrical insulation	3.5	mm	Thickness
HTS screen	0.2	mm	Thickness
Copper screen	1.5	mm	Thickness
Inner cryostat	18	mm	Radius
Cable length	1.0	mm	Length

$$\mathbf{A_1} \times \mathbf{C_1} \times \dot{\mathbf{V}}_1 = \mathbf{H_1} + [\mathbf{Y_1} \times \mathbf{V_1}] + [\mathbf{A_1} \times \mathbf{P_1}]. \tag{25}$$

Although equation (25) is quit similar to equation (24), its composing matrices are slightly different and their definitions can be found in appendix B. Similarly to the three-phase concentric design, such matrices should be adapted if sub-layers are considered. Table 6 presents the discretization for the *fdm* scheme and sub-layers configuration for the *tea* method used to perform the simulations with the single-phase design.

7. Modeling

7.1. Electrical network

A simple power system, as shown in figure 17(a), has been considered to investigate both cable designs under fault conditions. For the three-phase concentric one, a three phase grid has been assumed and for the single-phase design only one phase is modeled. Electrical resistances and inductances are set in order to achieve a nominal current of $200\,\mathrm{A_{RMS}}$ under normal operation and a fault current of about $20\,\mathrm{kA_{RMS}}$ in short-circuit conditions. For both cables, a symmetrical fault to the ground is considered. The grid is fed by a voltage source of $10\,\mathrm{kV_{RMS}}$. The switching sequence of S_1 and S_2 to emulate normal and fault conditions is illustrated in figure 17(b).

The transient period has been set to simulate 5 s. Figure 18 illustrate the first milliseconds of the simulated period, within which the fault takes place. Curves shown the current behavior for the three-phase grid. For the single phase analysis, only phase A is considered. Through these curves one can calculate the Joule losses in each phase conducting current.
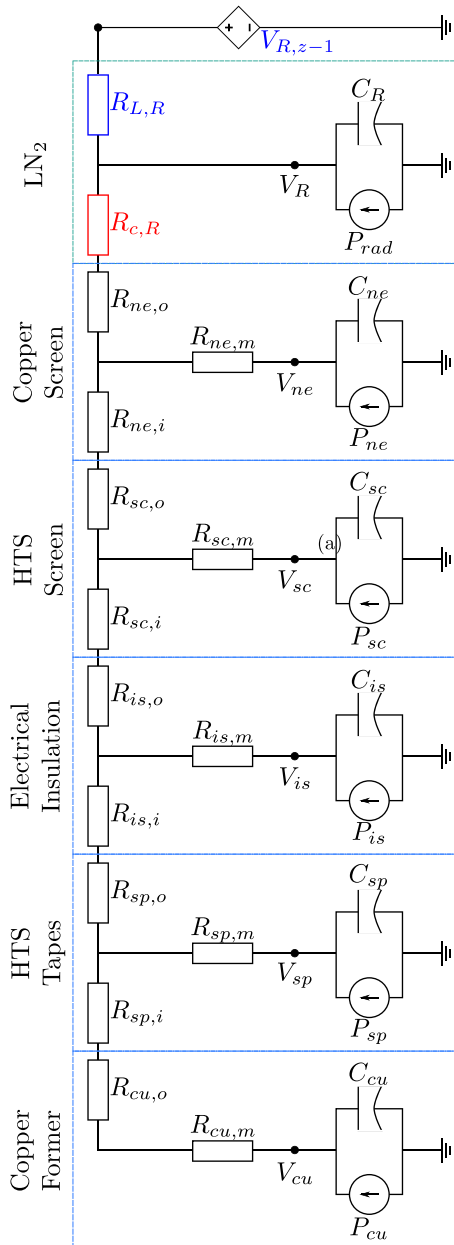
Figure 16. Thermal-network for the single-phase HTS cable design.

Table 6. Discretization of the single-phase design along radial direction.

	Number of elements	
Layer	*fdm*	*tea*
Copper former	825	2
HTS tapes	30	1
Electrical insulation	525	15
HTS screen	30	1
Copper screen	225	3

7.2. Simulation flowchart

Simulation codes developed for this manuscript were written using MatLab 2023a scripts. Nevertheless, they can be translated into any other programming language and embedded in any power system simulator which offers user
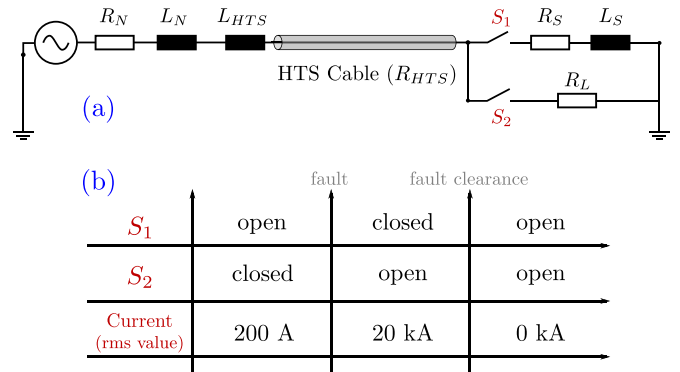

Figure 17. (a) Electrical grid configuration for transient simulation and (b) switching sequence of S_1 and S_2.
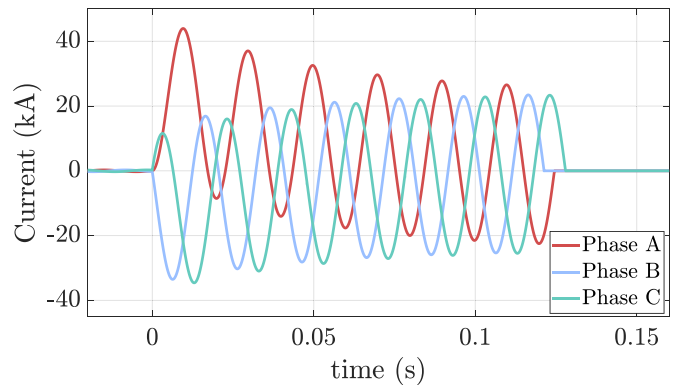

Figure 18. Simulated fault sequence alternating between normal operation and fault conditions.

defined models. The simulation flowchart shown in figure 19 enables the integration of the thermal-analogy model in different platforms without demanding for high computing performance. A computer equipped with Intel Core i9-12900K CPU at 3.20 GHz under Windows 10 operational system and 128 GB of memory RAM was used to produce the results shown in section 8.

The simulation starts with the definition of the electrical network where the cable is supposed to be integrated. By knowing these input parameters, one can determine and provide to the simulation script the geometric sizes and period to be simulated. This step is followed by the input of the physical properties of all materials composing the cable structure as well as the definition of the superconducting properties. Because the model considers the heat transport through the cooling medium, the discretization of the cable in Δz elements is necessary. Given these data, one now proceeds to create the thermal-networks for temperature calculations with those matrices presented in appendices A and B. Creating such matrices is a straightforward task which can be easily either manually settled up or through functions which speed up the process in case of several sub-layers. For the transient analysis, it is required to set the initial conditions of temperature. If such conditions are not known, then it is necessary to perform a simulation to determine it. In this work we have likewise applied the thermal-analogy model to find the initial temperatures in the cable. The determination of the steady AC regime follows
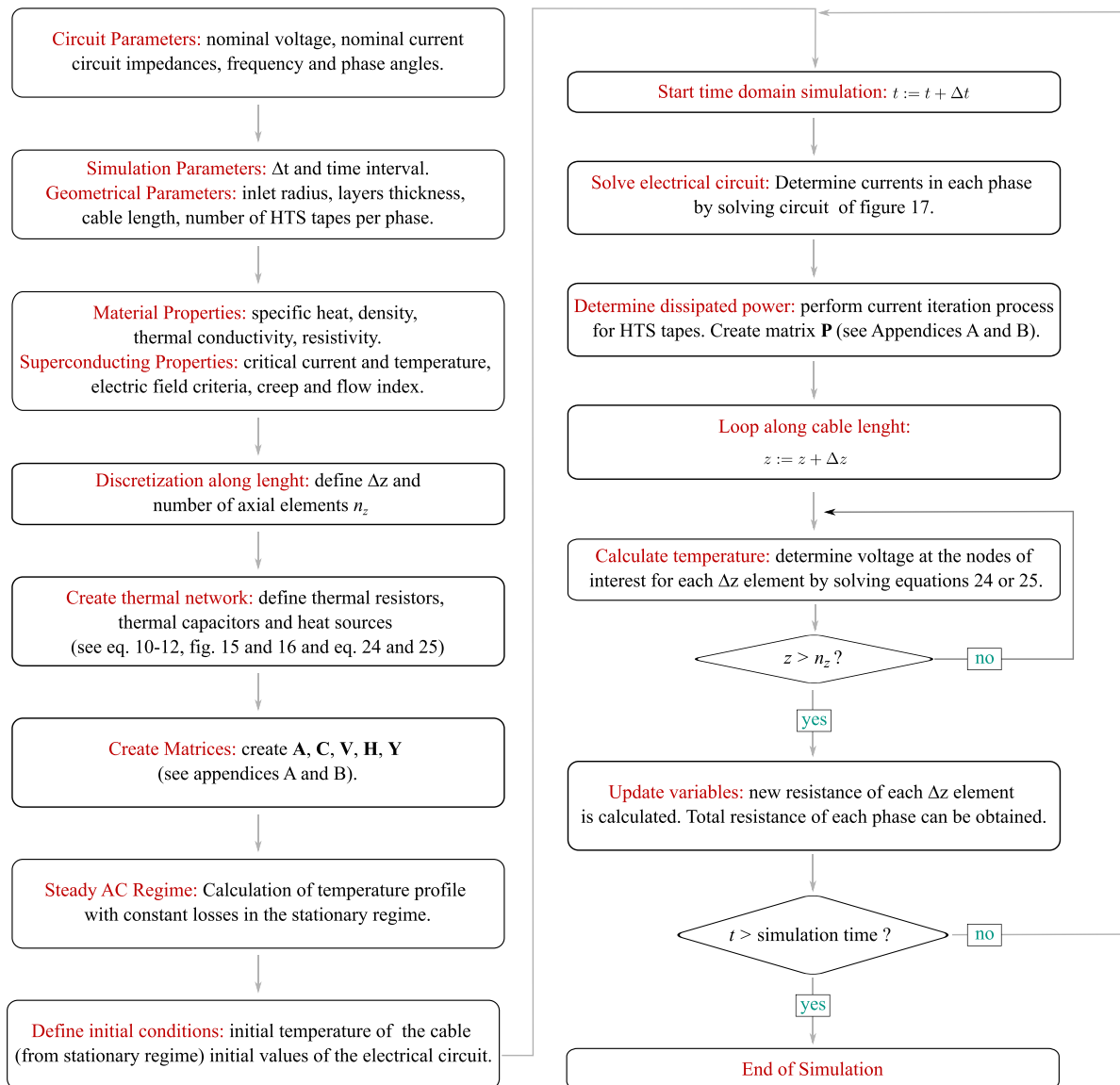
Circuit Parameters: nominal voltage, nominal current circuit impedances, frequency and phase angles.

Simulation Parameters: Δt and time interval.
Geometrical Parameters: inlet radius, layers thickness, cable length, number of HTS tapes per phase.

Material Properties: specific heat, density, thermal conductivity, resistivity.
Superconducting Properties: critical current and temperature, electric field criteria, creep and flow index.

Discretization along lenght: define Δz and number of axial elements n_z

Create thermal network: define thermal resistors, thermal capacitors and heat sources
(see eq. 10-12, fig. 15 and 16 and eq. 24 and 25)

Create Matrices: create **A**, **C**, **V**, **H**, **Y**
(see appendices A and B).

Steady AC Regime: Calculation of temperature profile with constant losses in the stationary regime.

Define initial conditions: initial temperature of the cable (from stationary regime) initial values of the electrical circuit.

Start time domain simulation: $t := t + \Delta t$

Solve electrical circuit: Determine currents in each phase by solving circuit of figure 17.

Determine dissipated power: perform current iteration process for HTS tapes. Create matrix **P** (see Appendices A and B).

Loop along cable lenght:
$z := z + \Delta z$

Calculate temperature: determine voltage at the nodes of interest for each Δz element by solving equations 24 or 25.

$z > n_z$? — no

yes

Update variables: new resistance of each Δz element is calculated. Total resistance of each phase can be obtained.

$t >$ simulation time ? — no

yes

End of Simulation

Figure 19. Simulation flowchart. Temperature dependence of physical properties is not considered.

the same logical reasoning of the transient one, just by considering zero or constant low electromagnetic losses in the cable. After finding the initial temperature values, one is able to determine the initial electrical parameters for the transient loop, as initial cable resistance and current values.

Once all initial conditions are determined, the time-loop starts. Firstly, the current flowing in the HTS tapes and copper (if present) is determined. That is achieved by solving the differential equation which governs the electrical grid where the HTS cable is connected. Here, it is possible to choose any numerical method able to solve such differential equation. In this work, the backward Euler method has been employed. At this point one must emphasize that such procedure can be skipped if the code is to be embedded in a power system simulator. In this case, values of the currents in the system are automatically found by the simulation software. Due to the high non-linearity of the HTS material, a current iteration process

is integrated in the simulation procedure. This iterative process is fully described in [51–53]. With the correct values of current in each layer, one can build the matrices which represent the losses in the cable.

Inside the time-looping, an axial loop is necessary to find the temperature values of the cable's layers in each Δz element. That is achieved by numerically solving equation (24) or (25). It is relevant to point out that operations involving matrix inversions are mandatory to obtain the solution of the thermal-network. If a suitable mathematical package is not available, a lower-upper (LU) decomposition can be deployed to perform these inversions.

Finally, with the new values of temperature inside the cable, the resistance of the HTS tapes can be updated. These values are used to calculate new values of electrical current in the system, restarting the time-loop over again. Such process continues until the predefined time of simulation is reached.
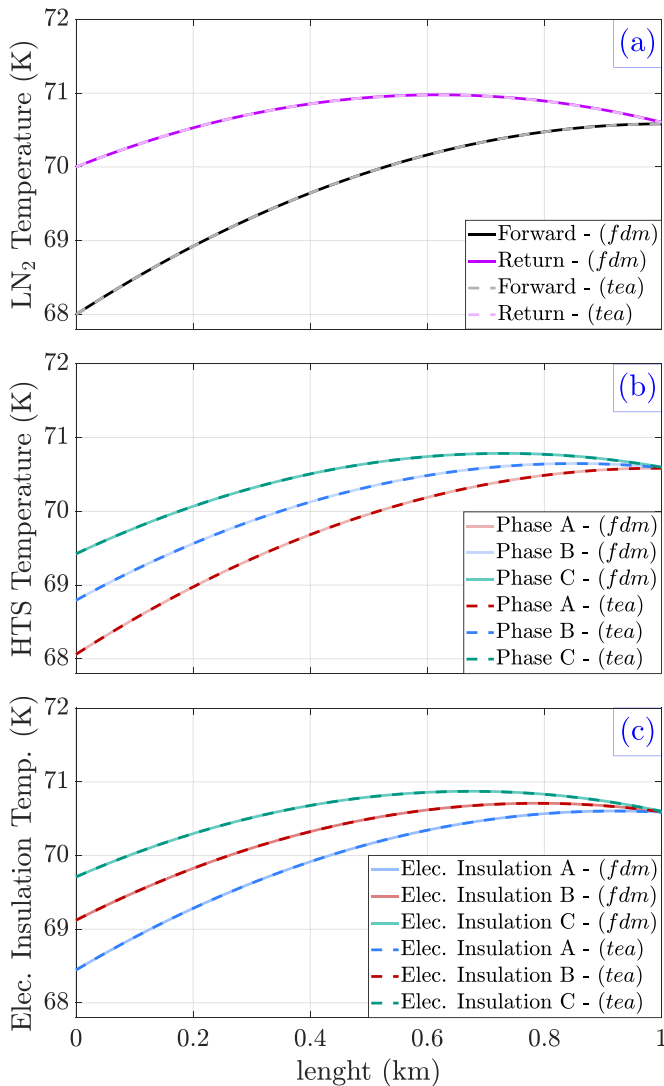
Figure 20. Results of steady AC regime for the three-phase concentric design given by *fdm* and *tea* methods. Temperature along length of (a) the forward and return flow of LN$_2$, (b) each phase composed of HTS tapes and (c) each electrical insulator inside the cable.

Figure 21. Results of steady AC regime for the single-phase design given by *fdm* and *tea* methods; Temperature along length of (a) HTS tapes transporting current and shielding (b) copper former and copper screen (c) forward flow of LN$_2$ and electrical insulation.

8. Results

8.1. Stationary

As mentioned before, the conditions of the cable under normal operation must be used as initial conditions in the transient regime. Results for the three-phase concentric design are shown in figure 20, where the comparison between the already published finite-difference method (*fdm*) [19] and the new thermal-electrical analogy (*tea*) developed along this manuscript is carried out. Steady AC regime results for the single-phase design are shown in figure 21. Cable layers are plotted in different windows to provide a better insight of the results.

As it can be observed, the *tea* method has a good accordance with that results delivered by the *fdm* scheme. Deviations between the two models are smaller than 0.5% for the steady regime analysis. Regarding the computer performance, it took
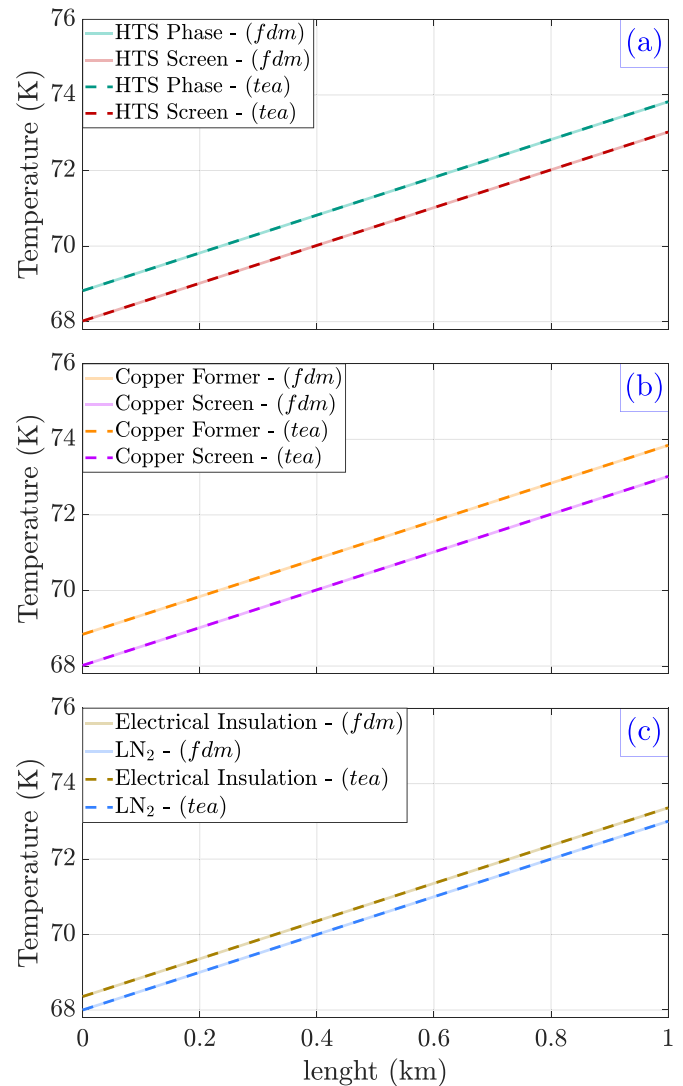
0.27 second for the *fdm* scheme to carry on the stationary calculations for the three-phase concentric design. The *tea* method delivered the same results after 0.07 second. For the single-phase design, the calculations were performed in 0.44 second using the *fdm* scheme and in 0.08 second with the *tea* method. Hence, it is clear that the *tea* method can deliver reliable results with less computational effort.

8.2. Transient

Transient thermal analysis are always challenging because of error propagations which takes place along the numerical integration. Aiming to minimize the propagation of errors, the multi-layer concept presented in section 4.3 and specified in tables 4 and 6 has been deployed.

Figures 22 and 23 show the currents in that circuit of figure 17(a) for each cable design respectively. No noticeable deviation has been identified between both methods. The
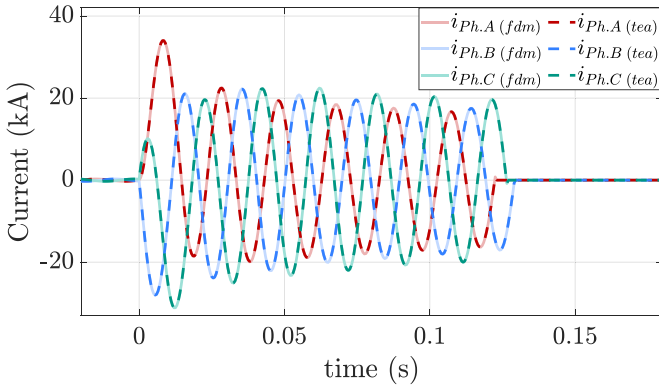
Figure 22. Comparison between the currents calculated for each phase of the three-phase concentric design with the *fdm* scheme and *tea* method.
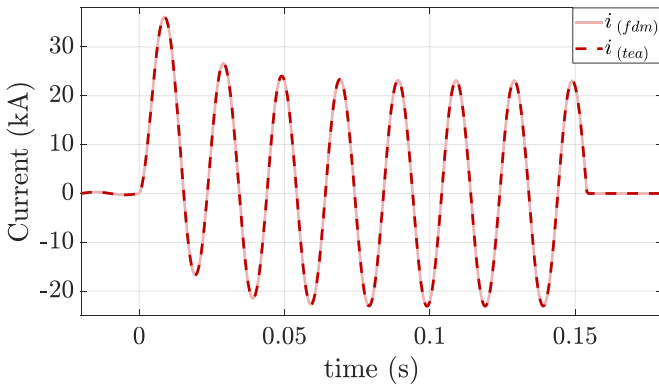

Figure 23. Comparison between the currents calculated for the single-phase design with the *fdm* scheme and *tea* method.

Figure 24. Comparison between the resistances calculated with *fdm* scheme and *tea* method for the three-phase concentric design: (a) the whole transient period and (b) only the first 200 ms.

Figure 25. Comparison between the resistances calculated with *fdm* scheme and *tea* method for the single-phase design. Only the first milliseconds are shown.

good agreement between the currents calculated by the compared methods arise from the good agreement between the calculated cable resistances, as shown in figures 24 and 25. Figure 24(a) presents the resistance of each phase of the three-phase concentric design for the whole transient period whereas figure 24(b) shows only the highlighted time-window of the first milliseconds of fault. A deviation of about 8% between the models can be noted for the resistance of phase C (R_C) around 4 s. Such a deviation however is not critical, since it has no major impact on the grid current (shown in figure 22). Figure 25 present the resistance behaviors of the single-phase cable design. Because this design is simpler than the three-phase concentric one, its resistance results are more accurate and no significant deviation regarding the *fdm* scheme has been found.

The results of resistance are of major importance for the *tea* method, since these are the values which will be delivered by the model to the power system simulator when considering the integration of HTS cables in electrical grids. A successful calculation of electrical resistance depends on the precise temperature calculation of the layers of the cable. Figure 26 compares the temperature values of each layer at the half length of the three-phase concentric cable ($L = 500$ m). As can be seen, the results of temperature for the HTS phases
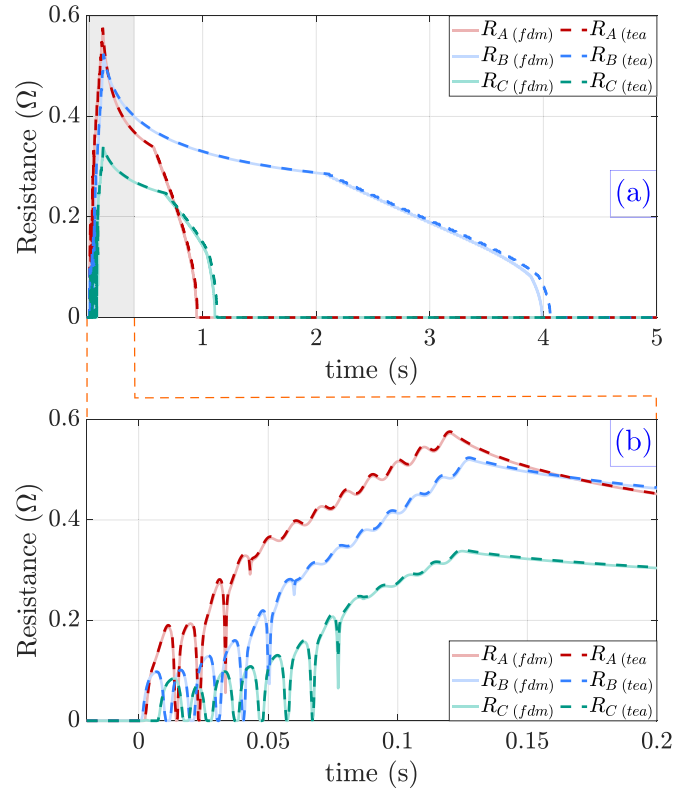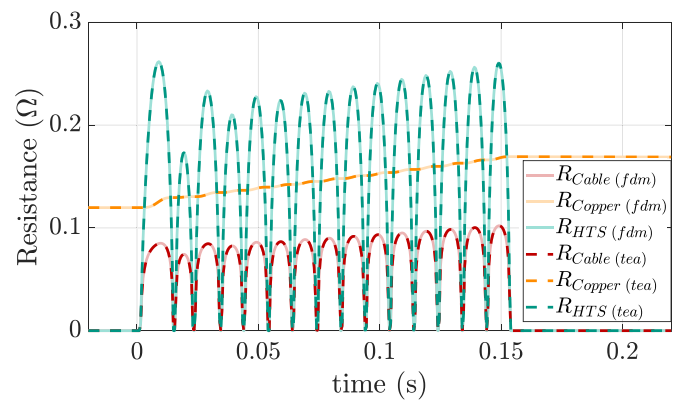
delivered by the *tea* method agree well with those calculated by the *fdm*. Small deviations are however observed when comparing the results of the electrical isolation. Between the onset of the fault and the end of the first second a deviation of about 3% took place for the temperature of isolation A, whereas for isolation B and C it was about 2.5% and 1%, respectively. After the first second all deviations are smaller than 1%.

Figure 27 shows the temperature results for the single-phase design at the half cable length. For this design, no
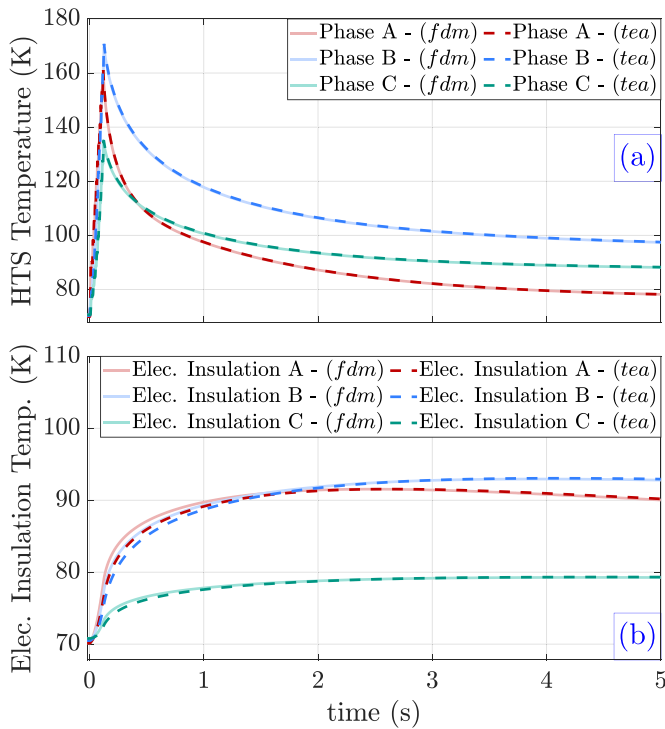
Figure 26. Comparison between temperature values at half cable length obtained with *fdm* scheme and *tea* method for the three-phase concentric design. Temperature of (a) HTS layers and (b) electrical insulators.
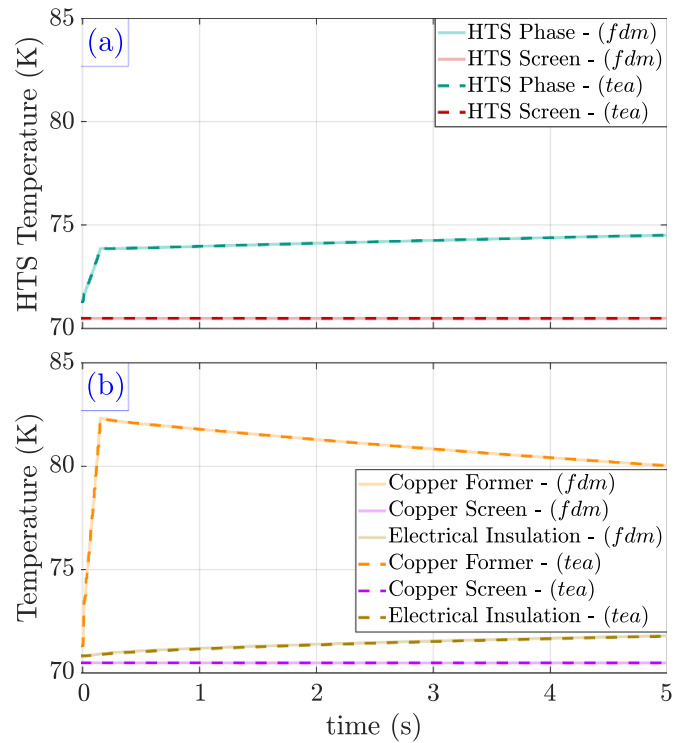

Figure 27. Comparison between temperature values at half cable length obtained with *fdm* scheme and *tea* method for the single-phase design. Temperature of (a) HTS layers and (b) electrical insulator, copper former and copper screen.

significant error values were identified. As can be observed, those curves delivered by the *tea* method coincide with the curves obtained by the *fdm* scheme. Dynamic changes of temperature over the length of the cable at four different time instants are depicted in figures 28–30 for the three-phase concentric design. One can recognize in figure 29(a) slight difference between both models for the temperature of the electrical insulators during the first milliseconds of the transient period. Such deviations correspond to those errors reported during the discussion of the results plotted in figure 26 and are not higher than 3% and vanish to values lower than 1% after the end of the fault period. A remarkable accordance between the *fdm* and *tea* approaches has been achieved for the transient behavior of the LN$_2$ flows temperatures (figure 30), where deviations lower than 0.5% where identified. These results validate the devel-

opment of the thermal-network model for the heat transport in the cooling media conducted in section 5.

Because the design of the single-phase cable is simpler than that of the three-phase concentric one, the agreement between the results delivered by the *fdm* and *tea* approaches in figures 31–33 are even better, with no significant deviations observed.

Regarding the computational effort, the *tea* method needs less time than the *fdm* approach to simulate and deliver the same results. As shown in table 7, simulations of the three-phase concentric performed with the *tea* method were about 4.4 times faster than those performed with the *fdm* one, whereas it was about 13.4 times faster for the single-phase geometry.
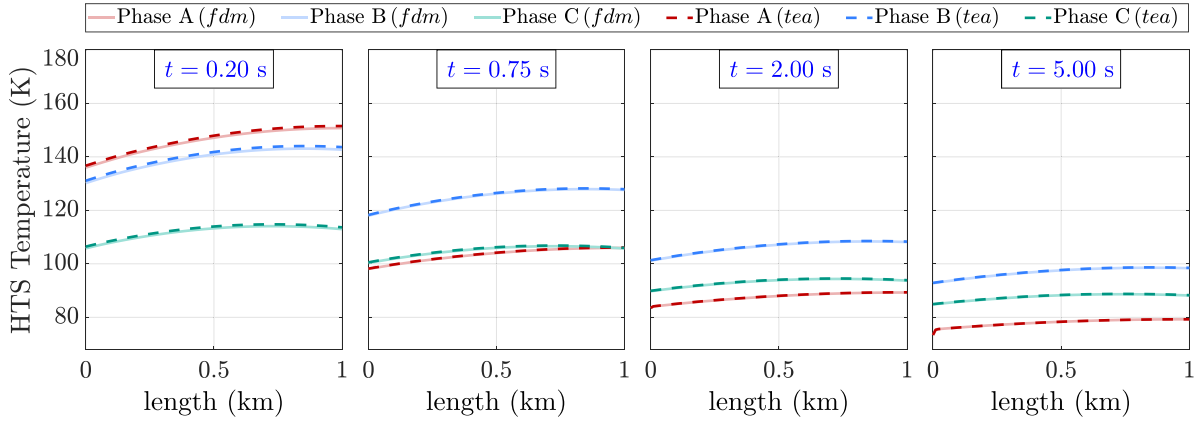
Figure 28. Temperature along the length of the cable for the HTS tapes in the three-phase concentric design. Comparison between results of *fdm* scheme and *tea* method.
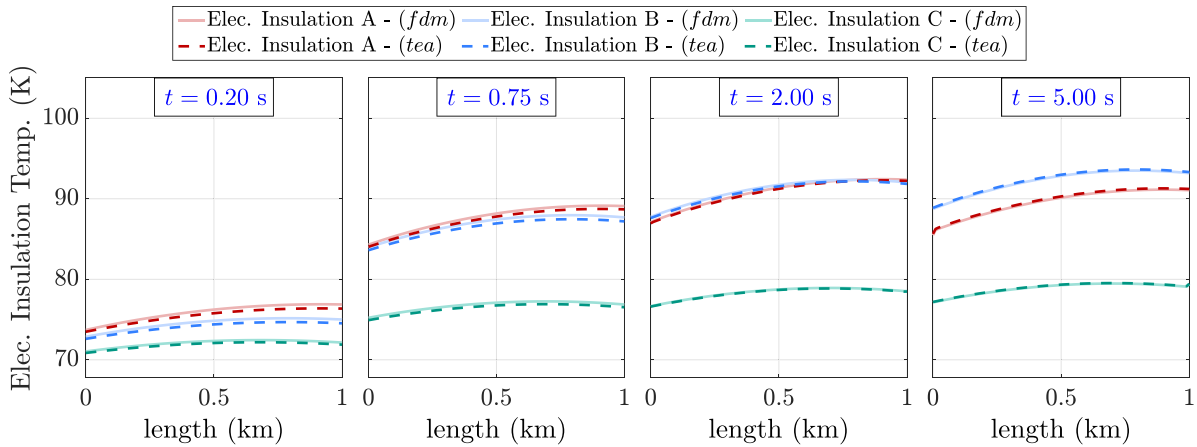

Figure 29. Temperature along the length of the cable for the electrical insulators in the three-phase concentric design. Comparison between results of *fdm* scheme and *tea* method.
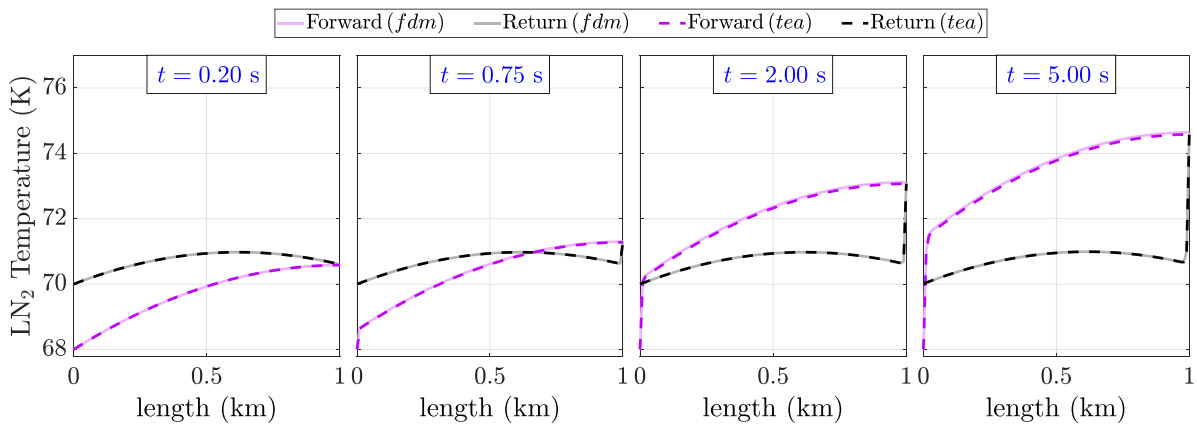

Figure 30. Temperature along the length of the cable for the forward and return LN$_2$ flow in the three-phase concentric design. Comparison between results of *fdm* scheme and *tea* method.
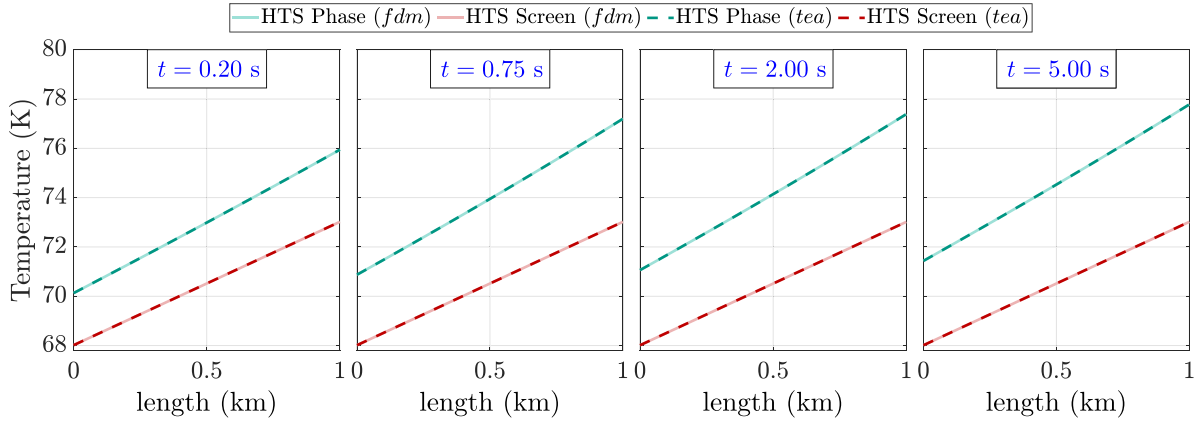
Figure 31. Temperature along the length of the cable for the HTS tapes in the single-phase design. Comparison between results of *fdm* scheme and *tea* method.
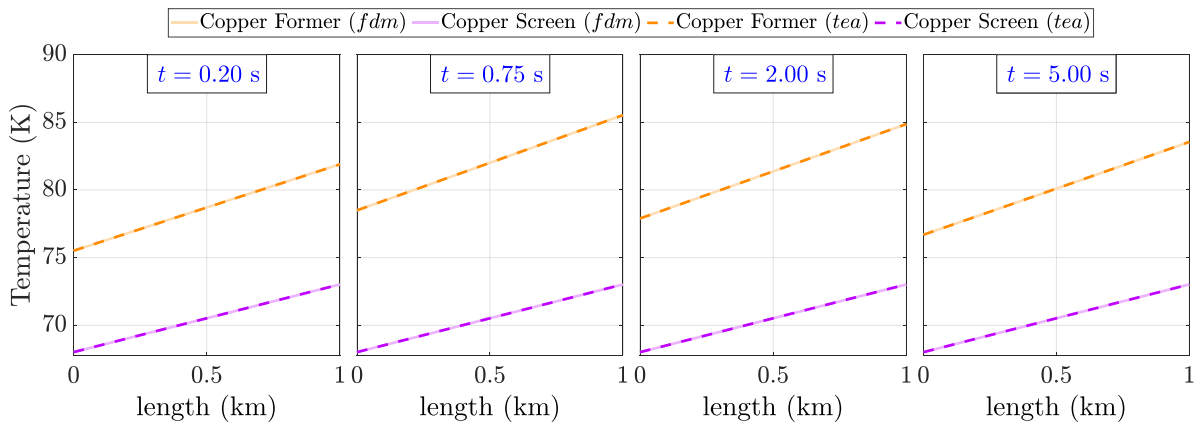

Figure 32. Temperature along the length of the cable for the copper former and copper screen in the single-phase design. Comparison between results of *fdm* scheme and *tea* method.
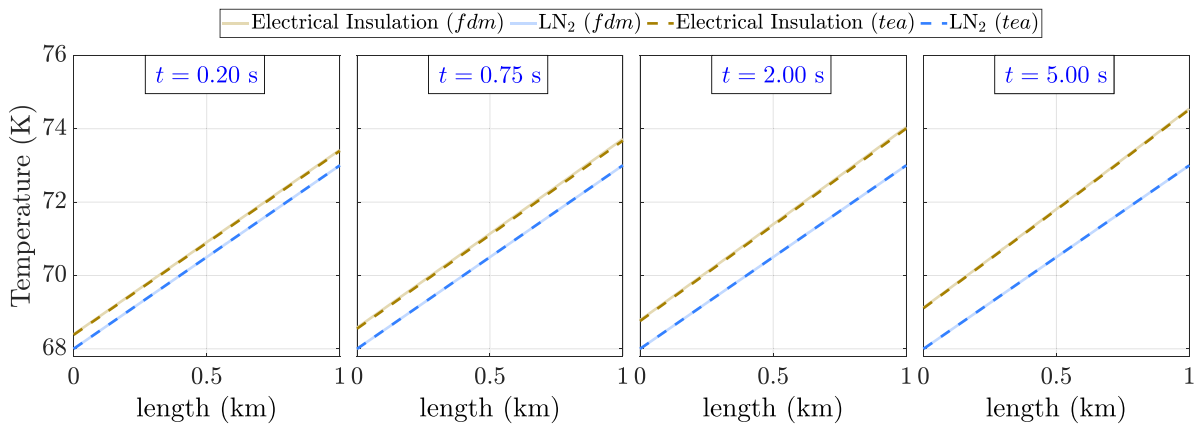

Figure 33. Temperature along the length of the cable for the forward flow of LN_2 flow and electrical insulation in the single-phase design. Comparison between results of *fdm* scheme and *tea* method.

Table 7. Computing time comparison[a].

	Three-phase concentric	Single-phase
fdm	1123 s	911 s
tea	256 s	68 s

[a] Computed by an Intel Core i9-12900K CPU 3.20 GHz equipped with 128 GB RAM computer.

9. Conclusions

In this work we have developed a light simulation model for superconducting power cables to be embedded in power system simulators. Although we have concentrated only in two different cables' designs, the model can be easily adapted for any other HTS cable concept. Including the proposed simulation scheme in electrical grid simulators takes place by either building the proper thermal-network (which is an undemanding task in such softwares) or by writing the simulation algorithm through user defined models (if available).

Based on thermal-networks, the method can deliver satisfactory results, considering that a proper multilayer configuration is chosen. Besides being faster and requiring less computational efforts, the model incorporates the boundary conditions between the cable's layers automatically. There is no need to specify the heat transfer at the interfaces, since it is a consequence when setting up the corresponding thermal-network. The proposed scheme to emulate the heat transport in the cooling media also delivered fulfilling outcomes. It is important to highlight that the *tea* method does not consider the axial heat transfer inside the solid layers, nevertheless it was able to provide a good agreement with the 2D *fdm* scheme. A further expansion of the *tea* method to include the axial heat transfer is possible and would enable the simulation of cases where the HTS tapes are to be inhomogeneous. Such expansion may be the next step on the development of suitable simulations tools for superconducting power cables.

Finally, we can state that the method presented in this paper is a reliable and stable simulation tool that can support the analysis of the influence of HTS cables in electrical grids. Integrating such a model in real time simulation environments is also envisioned.

Data availability statement

The data cannot be made publicly available upon publication because they are owned by a third party and the terms of use prevent public distribution. The data that support the findings of this study are available upon reasonable request from the authors.

Appendix A. Thermal network matrices of the three-phase concentric design

In this section, the matrices necessary to solve equation (24) are described. Matrices are only for single layer configuration. In the case of considering sub-layers (according to the multilayer concept), the matrices here presented should be expanded. For the upcoming matrices (A.22)–(A.27) the following relations are valid,

$$G_{L,F} = \frac{1}{R_{L,F}} \tag{A.1}$$

$$G_1 = \frac{1}{R_{c,F} + R_{fo,i}} \tag{A.2}$$

$$G_2 = \frac{1}{R_{fo,o} + R_{pa,i}} \tag{A.3}$$

$$G_3 = \frac{1}{R_{pa,o} + R_{ia,i}} \tag{A.4}$$

$$G_4 = \frac{1}{R_{ia,o} + R_{pb,i}} \tag{A.5}$$

$$G_5 = \frac{1}{R_{pb,o} + R_{ib,i}} \tag{A.6}$$

$$G_6 = \frac{1}{R_{ib,o} + R_{pc,i}} \tag{A.7}$$

$$G_7 = \frac{1}{R_{pc,o} + R_{ic,i}} \tag{A.8}$$

$$G_8 = \frac{1}{R_{ic,o} + R_{ne,i}} \tag{A.9}$$

$$G_9 = \frac{1}{R_{ne,o} + R_{c,R}} \tag{A.10}$$

$$G_{L,R} = \frac{1}{R_{L,R}} \tag{A.11}$$

$$G_{L1} = G_{L,F} + G_1 \tag{A.12}$$
$$G_{12} = G_1 + G_2 \tag{A.13}$$
$$G_{23} = G_2 + G_3 \tag{A.14}$$
$$G_{34} = G_3 + G_4 \tag{A.15}$$
$$G_{45} = G_4 + G_5 \tag{A.16}$$
$$G_{56} = G_5 + G_6 \tag{A.17}$$
$$G_{67} = G_6 + G_7 \tag{A.18}$$
$$G_{78} = G_7 + G_8 \tag{A.19}$$
$$G_{89} = G_8 + G_9 \tag{A.20}$$
$$G_{9L} = G_9 + G_{L,R} \tag{A.21}$$

$$A_3 = \begin{bmatrix} 1 & -G_1 R_{fo,m} & 0 & 0 & 0 & 0 & 0 & 0 & 0 & 0 \\ 0 & 1+G_{12}R_{fo,m} & -G_2 R_{ia,m} & 0 & 0 & 0 & 0 & 0 & 0 & 0 \\ 0 & -G_2 R_{fo,m} & 1+G_{23}R_{pa,m} & -G_3 R_{ia,m} & 0 & 0 & 0 & 0 & 0 & 0 \\ 0 & 0 & -G_3 R_{pa,m} & 1+G_{34}R_{ia,m} & -G_4 R_{pb,m} & 0 & 0 & 0 & 0 & 0 \\ 0 & 0 & 0 & -G_4 R_{ia,m} & 1+G_{45}R_{pb,m} & -G_5 R_{ib,m} & 0 & 0 & 0 & 0 \\ 0 & 0 & 0 & 0 & -G_5 R_{pb,m} & 1+G_{56}R_{ib,m} & -G_6 Rpc,m & 0 & 0 & 0 \\ 0 & 0 & 0 & 0 & 0 & -G_6 R_{ib,m} & 1+G_{67}R_{pc,m} & -G_7 R_{ic,m} & 0 & 0 \\ 0 & 0 & 0 & 0 & 0 & 0 & -G_7 R_{pc,m} & 1+G_{78}R_{ic,m} & -G_8 R_{ne,m} & 0 \\ 0 & 0 & 0 & 0 & 0 & 0 & 0 & -G_8 R_{ic,m} & 1+G_{89}R_{ne,m} & 0 \\ 0 & 0 & 0 & 0 & 0 & 0 & 0 & 0 & -G_9 R_{ne,m} & 1 \end{bmatrix} \tag{A.22}$$

$$
C_3 = \begin{bmatrix}
C_F & 0 & 0 & 0 & 0 & 0 & 0 & 0 & 0 & 0 \\
0 & C_{fo} & 0 & 0 & 0 & 0 & 0 & 0 & 0 & 0 \\
0 & 0 & C_{pa} & 0 & 0 & 0 & 0 & 0 & 0 & 0 \\
0 & 0 & 0 & C_{ia} & 0 & 0 & 0 & 0 & 0 & 0 \\
0 & 0 & 0 & 0 & C_{pb} & 0 & 0 & 0 & 0 & 0 \\
0 & 0 & 0 & 0 & 0 & C_{ib} & 0 & 0 & 0 & 0 \\
0 & 0 & 0 & 0 & 0 & 0 & C_{pc} & 0 & 0 & 0 \\
0 & 0 & 0 & 0 & 0 & 0 & 0 & C_{ic} & 0 & 0 \\
0 & 0 & 0 & 0 & 0 & 0 & 0 & 0 & C_{ne} & 0 \\
0 & 0 & 0 & 0 & 0 & 0 & 0 & 0 & 0 & C_R
\end{bmatrix} \tag{A.23}
$$

$$
\dot{V}_3 = \begin{bmatrix}
\dot{V}_F \\
\dot{V}_{fo} \\
\dot{V}_{pa} \\
\dot{V}_{ia} \\
\dot{V}_{pb} \\
\dot{V}_{ib} \\
\dot{V}_{pc} \\
\dot{V}_{ic} \\
\dot{V}_{ne} \\
\dot{V}_R
\end{bmatrix} \tag{A.24}
$$

$$
P_3 = \begin{bmatrix}
P_F \\
P_{fo} \\
P_{pa} \\
P_{ia} \\
P_{pb} \\
P_{ib} \\
P_{pc} \\
P_{ic} \\
P_{ne} \\
P_R
\end{bmatrix} \tag{A.25}
$$

$$
Y_3 = \begin{bmatrix}
-G_{L1} & G_1 & 0 & 0 & 0 & 0 & 0 & 0 & 0 & 0 \\
G_1 & -G_{12} & G_2 & 0 & 0 & 0 & 0 & 0 & 0 & 0 \\
0 & G_2 & G_{23} & G_3 & 0 & 0 & 0 & 0 & 0 & 0 \\
0 & 0 & G_3 & -G_{34} & G_4 & 0 & 0 & 0 & 0 & 0 \\
0 & 0 & 0 & G_4 & -G_{45} & G_5 & 0 & 0 & 0 & 0 \\
0 & 0 & 0 & 0 & G_5 & -G_{56} & G_6 & 0 & 0 & 0 \\
0 & 0 & 0 & 0 & 0 & G_6 & -G_{67} & G_7 & 0 & 0 \\
0 & 0 & 0 & 0 & 0 & 0 & G_7 & -G_{78} & G_8 & 0 \\
0 & 0 & 0 & 0 & 0 & 0 & 0 & G_8 & -G_{89} & G_9 \\
0 & 0 & 0 & 0 & 0 & 0 & 0 & 0 & G_9 & -G_{9L}
\end{bmatrix} \tag{A.26}
$$

$$
H_3 = \begin{bmatrix}
G_{L,F} V_{F,z-1} \\
0 \\
0 \\
0 \\
0 \\
0 \\
0 \\
0 \\
0 \\
-G_{L,R} V_{R,z-1}
\end{bmatrix} \tag{A.27}
$$

Appendix B. Thermal network matrices of the single-phase design

In this section, the matrices necessary to solve equation (25) are described. As in appendix A, matrices are only for single layer configuration and should be re-configured in the case of adding further sub-layers. For the upcoming matrices (B.12)–(B.17) the following relations are valid,

$$G_1 = \frac{1}{R_{cu,o} + R_{sp,i}} \tag{B.1}$$

$$G_2 = \frac{1}{R_{sp,o} + R_{is,i}} \tag{B.2}$$

$$G_3 = \frac{1}{R_{is,o} + R_{sc,i}} \tag{B.3}$$

$$G_4 = \frac{1}{R_{sc,o} + R_{ne,i}} \tag{B.4}$$

$$G_5 = \frac{1}{R_{ne,o} + R_{c,R}} \tag{B.5}$$

$$G_{L,R} = \frac{1}{R_{L,R}} \tag{B.6}$$

$$G_{12} = G_1 + G_2 \tag{B.7}$$
$$G_{23} = G_2 + G_3 \tag{B.8}$$
$$G_{34} = G_3 + G_4 \tag{B.9}$$
$$G_{45} = G_4 + G_5 \tag{B.10}$$
$$G_{5L} = G_5 + G_{L,R} \tag{B.11}$$

$$A_1 = \begin{bmatrix} 1+G_1R_{cu,m} & -G_1R_{sp,m} & 0 & 0 & 0 & 0 \\ -G_1R_{cu,m} & 1+G_{12}R_{sp,m} & -G_2R_{is,m} & 0 & 0 & 0 \\ 0 & -G_2R_{sp,m} & 1+G_{23}R_{is,m} & -G_3R_{sc,m} & 0 & 0 \\ 0 & 0 & -G_3R_{is,m} & 1+G_{34}R_{sc,m} & -G_4R_{ne,m} & 0 \\ 0 & 0 & 0 & -G_4R_{sc,m} & 1+G_{45}R_{ne,m} & 0 \\ 0 & 0 & 0 & 0 & -G_5R_{ne,m} & 1 \end{bmatrix} \tag{B.12}$$

$$C_1 = \begin{bmatrix} C_{cu} & 0 & 0 & 0 & 0 & 0 \\ 0 & C_{sp} & 0 & 0 & 0 & 0 \\ 0 & 0 & C_{is} & 0 & 0 & 0 \\ 0 & 0 & 0 & C_{sc} & 0 & 0 \\ 0 & 0 & 0 & 0 & C_{ne} & 0 \\ 0 & 0 & 0 & 0 & 0 & C_R \end{bmatrix} \tag{B.13}$$

$$Y_1 = \begin{bmatrix} -G_1 & G_1 & 0 & 0 & 0 & 0 \\ G_1 & -G_{12} & G_2 & 0 & 0 & 0 \\ 0 & G_2 & -G_{23} & G_3 & 0 & 0 \\ 0 & 0 & G_3 & -G_{34} & G_4 & 0 \\ 0 & 0 & 0 & G_4 & -G_{45} & G_5 \\ 0 & 0 & 0 & 0 & G_5 & -G_{5L} \end{bmatrix} \tag{B.14}$$

$$\dot{V}_1 = \begin{bmatrix} \dot{V}_{cu} \\ \dot{V}_{sp} \\ \dot{V}_{is} \\ \dot{V}_{sc} \\ \dot{V}_{ne} \\ \dot{V}_R \end{bmatrix} \tag{B.15}$$

$$P_1 = \begin{bmatrix} P_{cu} \\ P_{sp} \\ P_{is} \\ P_{sc} \\ P_{ne} \\ P_R \end{bmatrix} \tag{B.16}$$

$$H_1 = \begin{bmatrix} 0 \\ 0 \\ 0 \\ 0 \\ 0 \\ G_{L,R}V_{R,z-1} \end{bmatrix} \tag{B.17}$$

ORCID iDs

Wescley T B de Sousa https://orcid.org/0000-0002-0537-4568
João Murta-Pina https://orcid.org/0000-0002-9283-8497
Antonio Morandi https://orcid.org/0000-0002-1845-4006
Mathias Noe https://orcid.org/0009-0006-5870-968X

References

[1] Wang X, Ishiyama A, Ohya M and Fujiwara N 2011 *IEEE Trans. Appl. Supercond.* **21** 1013–6
[2] Sohn S H *et al* 2005 *J. Phys.: Conf. Ser.* **43** 885–8
[3] Sohn S *et al* 2010 *Physica* C **470** 1567–71
[4] Allais A, West B, Frentzas F, Lallouet N, Marzahn E, Ross M and Saugrain J M 2023 Recent Superconducting Cable Installation in Chicago Paves the Way for a Resilient Electric Grid (REG) *27th Int. Conf. on Electricity Distribution (CIRED 2023)* vol 2023 pp 2793–9
[5] Maguire J F, Yuan J, Romanosky W, Schmidt F, Soika R, Bratt S, Durand F, King C, McNamara J and Welsh T E 2011 *IEEE Trans. Appl. Supercond.* **21** 961–6
[6] Stemmle M, Merschel F, Noe M and Hobl A 2013 AmpaCity - installation of advanced superconducting 10 kV system in city center replaces conventional 110 kV cables *2013 IEEE Int. Conf. on Applied Superconductivity and Electromagnetic Devices (ASEMD)* (IEEE) pp 323–6
[7] Stemmle M, Merschel F, Noe M and Hobl A 2013 AmpaCity project - worldwide first superconducting cable and fault current limiter installation in a german city center *22nd Int. Conf. and Exhibition on Electricity Distribution (CIRED 2013)* pp 1–4
[8] Prusseit W and Bach R 2021 *Transformer Mag.* **8** 38–43
[9] Yang B, Kang J, Lee S, Choi C and Moon Y 2015 *IEEE Trans. Appl. Supercond.* **25** 1–5
[10] Hajiri G, Berger K, Dorget R, Lévêque J and Caron H 2022 *Supercond. Sci. Technol.* **35** 024003
[11] Watanabe H *et al* 2017 *IOP Conf. Ser.: Mater. Sci. Eng.* **171** 012116
[12] Zhang D, Dai S, Zhang F, Zhu Z, Xu X, Zhou W, Teng Y and Lin L 2015 *IEEE Trans. Appl. Supercond.* **25** 1–4
[13] Magnusson N *et al* 2023 *IEEE Trans. Appl. Supercond.* **21** 1–5
[14] Allais A *et al* 2024 *IEEE Trans. Appl. Supercond.* **34** 1–7
[15] Shen B, Coombs T and Grilli F 2019 *IEEE Trans. Appl. Supercond.* **29** 1–5
[16] Douine B, Netter D, Leveque J and Rezzoug A 2002 *IEEE Trans. Appl. Supercond.* **12** 1603–6

[17] Sytnikov V E, Shutov K A, Polyakova N V, Fetisov S S, Nosov A A and Vysotsky V S 2009 *IEEE Trans. Appl. Supercond.* **19** 1706–9
[18] Savoldi L, Placido D and Viarengo S 2022 *Supercond. Sci. Technol.* **35** 044001
[19] de Sousa W T B, Shabagin E, Kottonau D and Noe M 2020 *Supercond. Sci. Technol.* **34** 015014
[20] Del-Rosario-Calaf G, Lloberas-Valls J, Sumper A, Granados X and Villafafila-Robles R 2013 *IEEE Trans. Appl. Supercond.* **23** 5401204–5401204
[21] de Sousa W T B, Kottonau D, Bock J and Noe M 2018 *IEEE Trans. Appl. Supercond.* **28** 5400105
[22] Ha S, Kim S, Kim J, Park M, Yu I, Lee S, Sim K and Kim A 2013 *IEEE Trans. Appl. Supercond.* **23** 5400104
[23] Ha S-K, Kim S-K, Kim J-G, Park M, Yu I-K, Lee S, Kim J-H and Sim K 2015 *J. Electr. Eng. Technol.* **10** 2083–8
[24] Xiang W, Yuan W, Xu L, Hodge E, Fitzgerald J, McKeever P and Bell K 2022 *IEEE Trans. Energy Convers.* **37** 377–88
[25] Morandi A 2015 *Supercond. Sci. Technol.* **28** 123001
[26] Li X *et al* 2023 *Supercond. Sci. Technol.* **36** 125001
[27] Morandi A, Gholizad B, Stieneker M, Stagge H and Doncker R W D 2016 *IEEE Trans. Appl. Supercond.* **26** 1–10
[28] de Sousa W T B, Polasek A, Dias R, Matt C F T and de Andrade J R 2014 *Cryogenics* **62** 97–109
[29] dos Santos G, Bitencourt A, Queiroz A T, Martins F G R, Sass F, Dias D H N, Sotelo G G and Polasek A 2021 *Supercond. Sci. Technol.* **34** 045009
[30] Guillen D, Salas C, Trillaud F, Castro L M, Queiroz A T and Sotelo G G 2020 *Electr. Power Syst. Res.* **186** 106419
[31] Dong Q, de Sousa W T B, Geng J, Zhang X, Zhang H, Shen B and Coombs T 2019 *IEEE Trans. Appl. Supercond.* **29** 1–7
[32] Jena P and Gupta R 2022 *Heat Mass Transfer* 1–12
[33] Arsenio P, Murta-Pina J, Porto A, Alvarez A and Catarino I 2018 *IEEE Trans. Appl. Supercond.* **28** 5602209
[34] Lawson D I and McGuire J H 1956 *P. I. Mech. Eng.* **167** 275–90
[35] Robertson A F and Gross D 1958 *J. Res. Natl Bur. Stand.* **61** 105–15
[36] Bergman T L and Incropera F P 2011 *Fundamentals of Heat and Mass Transfer* (Wiley)
[37] Juha Pyrhoenen T J and Hrabovcova V 2008 *Design of Rotating Electrical Machines* 1st edn (Wiley)
[38] Ozisik M N 1985 *Heat Transfer A Basic Approach* 1st edn (McGraw-Hill)
[39] Perez I J and Kassakian J G 1979 *Electr. Mach. Power Syst.* **3** 285–303
[40] Kuehbacher D, Kelleter A and Gerling D 2013 An improved approach for transient thermal modeling using lumped

parameter networks *2013 Int. Electric Machines and Drives Conf.* pp 824–31

[41] Gerling D and Dajaku G 2005 Novel lumped-parameter thermal model for electrical systems *2005 European Conf. on Power Electronics and Applications* pp 1–10

[42] Mejuto C, Mueller M, Shanel M, Mebarki A, Reekie M and Staton D 2008 Improved synchronous machine thermal modelling *2008 18th Int. Conf. on Electrical Machines* pp 1–6

[43] Anderson B 2013 Lumped parameter thermal modelling of electric machines *Master's Thesis* Chalmers University of Technology

[44] Su R *et al* 2019 *IEEE Trans. Appl. Supercond.* **29** 4802005

[45] Mellor P H, Roberts D and Turner D R 1991 *IEE Proc.* B **138** 205–18

[46] Li K, Wang S, He Z, Wang K and Sullivan J P 2012 Radial maximum thermal network based on hollow cylinder structure geometry *IEEE 10th Int. Conf. on Industrial Informatics* pp 706–12

[47] Shoujun S, Weiguo L, Peitsch D and Schaefer U 2010 *Chin. J. Aeronaut.* **23** 216–26

[48] Lee B-H, Kim K-S, Jung J-W, Hong J-P and Kim Y-K 2012 *IEEE Trans. Magn.* **48** 2949–52

[49] Rouhani H, Faiz J and Lucas C 2007 *Math. Comput. Modelling* **45** 625–38

[50] VDI-Gesellschaft Verfahrenstechnik und Chemieingenieurwesen 2013 *VDI Heat Atlas* (*VDI-WäRmeatlas*) (Springer)

[51] de Sousa W T B 2015 Transient simulations of superconducting fault current limiters *PhD Thesis* COPPE/UFRJ

[52] Mäder O 2012 Simulationen und Experimente zum Stabilitätsverhalten von HTSL-Bandleitern *PhD Thesis* Karlsruher Institut fúr Technologie, Fakultät für Elektrotechnik und Informationstechnik

[53] Butzke U 1996 Simulationen resistiver hochtemperatur-supraleitender Strombegrenzer mit Hilfe der Finiten-Differenzen Methode diplomarbeit, Universitaet Hannover - Institut fuer Elektrische Energieversorgung